PAPER P-695

SOLAR FLUX, AND "TOTAL" PARTICLE AND 0_2 DENSITY, IN UPPER ATMOSPHERE

Alan J. Grobecker

September 1971

IDA
INSTITUTE FOR DEFENSE ANALYSES
SCIENCE AND TECHNOLOGY DIVISION

DISCLAIMER NOTICE

THIS DOCUMENT IS THE BEST QUALITY AVAILABLE.

COPY FURNISHED CONTAINED A SIGNIFICANT NUMBER OF PAGES WHICH DO NOT REPRODUCE LEGIBLY.

UNCLASSIFIED
Security Classification

DOCUMENT CONTROL DATA - R & D
(Security classification of title, body of abstract and indexing annotation must be entered when the overall report is classified)

1. ORIGINATING ACTIVITY (Corporate author)
INSTITUTE FOR DEFENSE ANALYSES
400 Army-Navy Drive
Arlington, Virginia 22202

2a. REPORT SECURITY CLASSIFICATION
UNCLASSIFIED

2b. GROUP
--

3. REPORT TITLE
Solar Flux, and "Total" Particle and O_2 Density, in Upper Atmosphere

4. DESCRIPTIVE NOTES (Type of report and inclusive dates)
Paper P-695 - September 1971

5. AUTHOR(S) (First name, middle initial, last name)
Alan J. Grobecker

6. REPORT DATE
September 1971

7a. TOTAL NO. OF PAGES
83

7b. NO. OF REFS
36

8a. CONTRACT OR GRANT NO.
IDA Independent Research Program (0242) and Contract DAHC15 67C 0011

b. PROJECT NO.
Task T-58

c.

d.

9a. ORIGINATOR'S REPORT NUMBER(S)
P-695

9b. OTHER REPORT NO(S) (Any other numbers that may be assigned this report)
None

10. DISTRIBUTION STATEMENT
Approved for public release; distribution unlimited.

11. SUPPLEMENTARY NOTES
N/A

12. SPONSORING MILITARY ACTIVITY
Advanced Research Projects Agency
Arlington, Virginia 22209

13. ABSTRACT

Solar flux, and "total" particle and O_2 density distribution, in the upper mesosphere and lower thermosphere (70- to 150-km region) are described. Respective distributions were determined from solar flux intensities measured by ion chambers in three rocket vehicles launched on 21 February 1966 from North America (two at Eglin Gulf Test Range, Florida, and one at Fort Churchill, Manitoba). Method of determining density distributions is given.

Solar flux outside and inside the absorbing atmosphere was measured for the following wave bands: 1-20Å (X ray), 1140-1260Å (mainly hydrogen Lyman-α line at 1215.6Å), and 1325-1475Å (Schumann-Runge continuum). Distributions of O_2 and "total" particle density are based on the solar flux absorption in the sensible atmosphere.

Results of solar flux measurements compare, in general, with results obtained elsewhere. Estimated errors vary from 10 to 100 percent. Density results also agree generally with those of other experimenters (using similar or other techniques), except for one striking difference: a step of O_2 density exists at 113 ± 7 km altitudes. This step, which to our knowledge has not been reported elsewhere, is described theoretically. Its existence is also confirmed by electron density data derived by ionosonde at each launch site.

DD FORM 1 NOV 68 1473

UNCLASSIFIED
Security Classification

14 KEY WORDS	LINK A		LINK B		LINK C	
	ROLE	WT	ROLE	WT	ROLE	WT
solar flux absorption in sensible atmosphere						
solar flux intensities in upper atmosphere						
O_2 and "total" particle density in upper atmosphere						

The work reported in this document was conducted under contract DAHC15 67 C 0011 for the Department of Defense. The publication of this IDA Paper does not indicate endorsement by the Department of Defense, nor should the contents be construed as reflecting the official position of that agency.

PAPER P-695

SOLAR FLUX, AND "TOTAL" PARTICLE AND 0_2 DENSITY, IN UPPER ATMOSPHERE

Alan J. Grobecker

September 1971

INSTITUTE FOR DEFENSE ANALYSES
SCIENCE AND TECHNOLOGY DIVISION
400 Army-Navy Drive, Arlington, Virginia 22202

IDA Independent Research Program (0242) and
Contract DAHC15 67 C 0011
Task T-58

ACKNOWLEDGMENTS

The effort for which results are reported here was funded by the Office of Naval Research, National Science Foundation, National Aeronautical and Space Administration, North American Aviation, Inc., and the Institute for Defense Analyses.

Special thanks are due to Prof. G. J. F. MacDonald and Dr. Herbert Friedman for their continuous encouragement. Thanks are also due Dr. T. A. Chubb, E. T. Byram, C. Y. Johnson, J. Siomkajlo, Dr. J. Meekins, A. Unzicker, and R. Kreplin of the Naval Research Laboratory; G. McCue, Dr. J. Zimmermann, C. Lotstein, C. Vok, B. Kotick, and A. Okuda of North American Aviation, Inc., and B. DeFlorio of the Institute for Defense Analyses. The cooperation of R. J. Cormier of AFCRL Laboratory, Bedford, Massachusetts, in furnishing riometer data and of J. W. Wright of ESSA Research Laboratory in making ionosonde measurements and computing electron density distributions is appreciated.

ABSTRACT

Solar flux, and "total" particle and O_2 density distribution, in the upper mesosphere and lower thermosphere (70- to 150-km region) are described. Respective distributions were determined from solar flux intensities measured by ion chambers in three rocket vehicles launched on 21 February 1966 from North America (two at Eglin Gulf Test Range, Florida, and one at Fort Churchill, Manitoba). Method of determining density distributions is given.

Solar flux outside and inside the absorbing atmosphere was measured for the following wave bands: 1-20Å (X ray), 1140-1260Å (mainly hydrogen Lyman-α line at 1215.6Å), and 1325-1475Å (Schumann-Runge continuum). Distributions of O_2 and "total" particle density are based on the solar flux absorption in the sensible atmosphere.

Results of solar flux measurements compare, in general, with results obtained elsewhere. Estimated errors vary from 10 to 100 percent. Density results also agree generally with those of other experimenters (using similar or other techniques), except for one striking difference: a step of O_2 density exists at 113 ± 7 km altitudes. This step, which to our knowledge has not been reported elsewhere, is described theoretically. Its existence is also confirmed by electron density data derived by ionosonde at each launch site.

CONTENTS

FIGURES

TABLES

I. INTRODUCTION

Experiments described in this paper were undertaken as a contribution to an on-going scientific effort to study the upper atmosphere in the 70- to 150-km altitude region (upper mesosphere and lower thermosphere).

Numerous factors make this part of the upper atmosphere an interesting one to study. For example, most modes of radio communication are sensitive to density distributions, temperature, and motions (winds and turbulences) found here. Also, density distributions and temperature in the upper mesosphere control the ventilation upward of the stratosphere and mesosphere--significant regions in the light of predicted pollution by exhaust gases of supersonic transport vehicles and rockets. In the lower thermosphere, density distribution at the higher altitudes fluctuates widely as compared with that at the lower altitudes where density fluctuations are smaller. The strong fluctuations at these higher altitudes can strongly affect the temporal changes in orbital characteristics of earth satellites whose perigees may be low.

Study of this region, in which geophysical processes are many and varied, has been handicapped in the past because various experimental techniques that have been effective in studying atmospheric characteristics above and below the region proved ineffective within the region.

Experimental data were obtained by three rocket vehicles (Grobecker, 1967a), launched on 21 February 1966 by the Naval Research Laboratory (NRL). Two lifted off at Eglin Gulf Test Range, Florida, and one at Fort Churchill, Manitoba. Launch locations, times, settings, sun positions, and apogee information are given in Table 1.

TABLE 1. GEOMETRY AND TIMES OF ROCKET VEHICLE EXPERIMENTS

Rocket Vehicle Experiment (NRL)	Launch Location			Launch Time		Launcher Setting		Sun Position			Apogee	
	Place	Latitude deg min	Longitude deg min	AST hr min	CST hr min	Az (deg)	Elev. (deg)	Decl. (deg)	Zenith Angle (deg)	Az Angle (deg)	CST hr min	Altitude km
NC7.178	Ft. Churchill, Manitoba, Canada	58 44 N	93 04 W	13 57.2	14 23.17	86.9	82.5	S10.5	73.2[a]	149.7	14 26.67	196.4
NC7.180	Eglin, Fla. U.S.A.	30 24 N	86 43 W	13 56.5	13 57.00	159.6	86.6	S10.5	49.5[b]	141.1	14 00.43	187.4
NC7.181	Eglin, Fla. U.S.A.	30 24 N	86 43 W	07 09.1	07 09.59	205.3	83.3	S10.6	80.7[c]	108.1	07 10.00	184.9

Passage of rocket vehicles through 100-km altitude occurred about 70 sec after launch.

AST = Apparent Solar Time

CST = Central Standard Time = GMT - 6 hr

GMT = Greenwich Mean Time

a. Variation of 73^{o} 11′ to 73^{o} 17′

b. Variation of 49^{o} 33′ to 49^{o} 41′

c. Variation of 81^{o} 04′ to 80^{o} 19′

Each rocket vehicle contained four pairs of ion chambers: two pairs sensitive to vacuum ultraviolet rays (Grobecker, 1967b) and two sensitive to X-radiation (Grobecker, 1967c). Molecular oxygen density and "total" particle density in the upper mesosphere and lower thermosphere were determined from the chambers' measurements of the sensible atmosphere's absorption of solar radiation along a near-vertical trajectory through the region.

Solar flux absorption inside the sensible atmosphere and solar flux intensities outside the sensible atmosphere were determined for three wave bands yielding the most useful information: 1-20Å (X ray), 1140-1260Å [mainly hydrogen Lyman-α (H Ly-α)] line at 1215.6Å, and 1325-1475Å [Schumann-Runge (SR)] continuum.

Absorption of solar flux by the O_2 molecule, at the measurement altitudes of the experiments, was determined at the H Ly-α line and in the SR continuum. Absorption by oxygen and nitrogen atoms, either free or bound in molecular form, was determined in the 1-20Å wave band.

Solar flux in each wave band was measured by two ion chambers (detectors A & B) in each rocket vehicle. Originally, it was planned to determine solar flux in the 44-60Å wave band, and two detectors in each rocket vehicle measured intensities in this band during the experiments. However, results from these detectors were considered not useful since the 44-60Å determination proved sensitive to errors in 1-20Å flux determinations. Consequently, these particular results are not discussed in the paper.

Throughout this paper, detectors for each of the three wave bands providing usable data are referred to either by wave band (i.e., 1-20Å, H Ly-α, and SR detectors corresponding to the respective wave band ranges) or by the channel through which measurement data were telemetered (i.e., Channel 14 detector for 1-20Å, Channel 15 for H Ly-α, and Channel 18 for SR).

Vertical profiles of electron density were determined continuously by ionosonde at each launch site during launch periods.

Solar flux determinations are discussed in Section II of this paper. They are described in terms of flux absorption inside the sensible atmosphere and flux intensities outside it, flux computations, flux as a function of altitude, and error contributions in the flux measurements.

"Total" particle and O_2 density distribution, based on the solar flux determination, is discussed in Section III. This is presented in terms of analyzing solar flux absorption data, computing density values as a function of altitude, and interpreting the experimental data from the geophysical standpoint.

Information related to observations of solar emission constancy during the experimental period is presented in Appendix A. Material amplifying density computations in Section III is given in Appendix B.

II. SOLAR FLUX DETERMINATION

A. FLUX ABSORPTION WITHIN THE ATMOSPHERE

Individual results of the three rocketborne experiments to determine the absorption of solar flux in each of the three wave bands yielding useful information are given in Figs. 1, 2, and 3. Flux values within the sensible absorbing atmosphere are shown as functions of altitude, determined from the ion current of each of two detectors (A & B) turned toward the sun, one after the other, as the rocket vehicle spun in its near-vertical trajectory. Heavy lines indicate the values of solar flux believed with confidence to be important in determining density values; thin lines indicate flux determinations in which there is lesser confidence in their importance. The diminishment of confidence is based on several criteria:

1. Slope of the flux value's logarithm versus integrated number density (absorbing particles, per cm^2, of gas between the sun and detector) changes abruptly, indicating a sharp unexplainable change of mean absorption coefficient.
2. Flux values are physically inconsistent.
3. Density determinations from the several flux bands are mutually inconsistent.

Information content of data plotted in Figs. 1, 2, and 3 contains only frequencies below 0.125 Hz.

Examples of how these criteria are applied are revealed by the curves in Figs. 1, 2, and 3. A change of slope in the semilog plot of flux measured by Channel 15 at about 104 km is noted in records of experiments NC7.178 and NC7.181, and at about 93 km in the record of NC7.180. In determining density from the H Ly-α flux values at

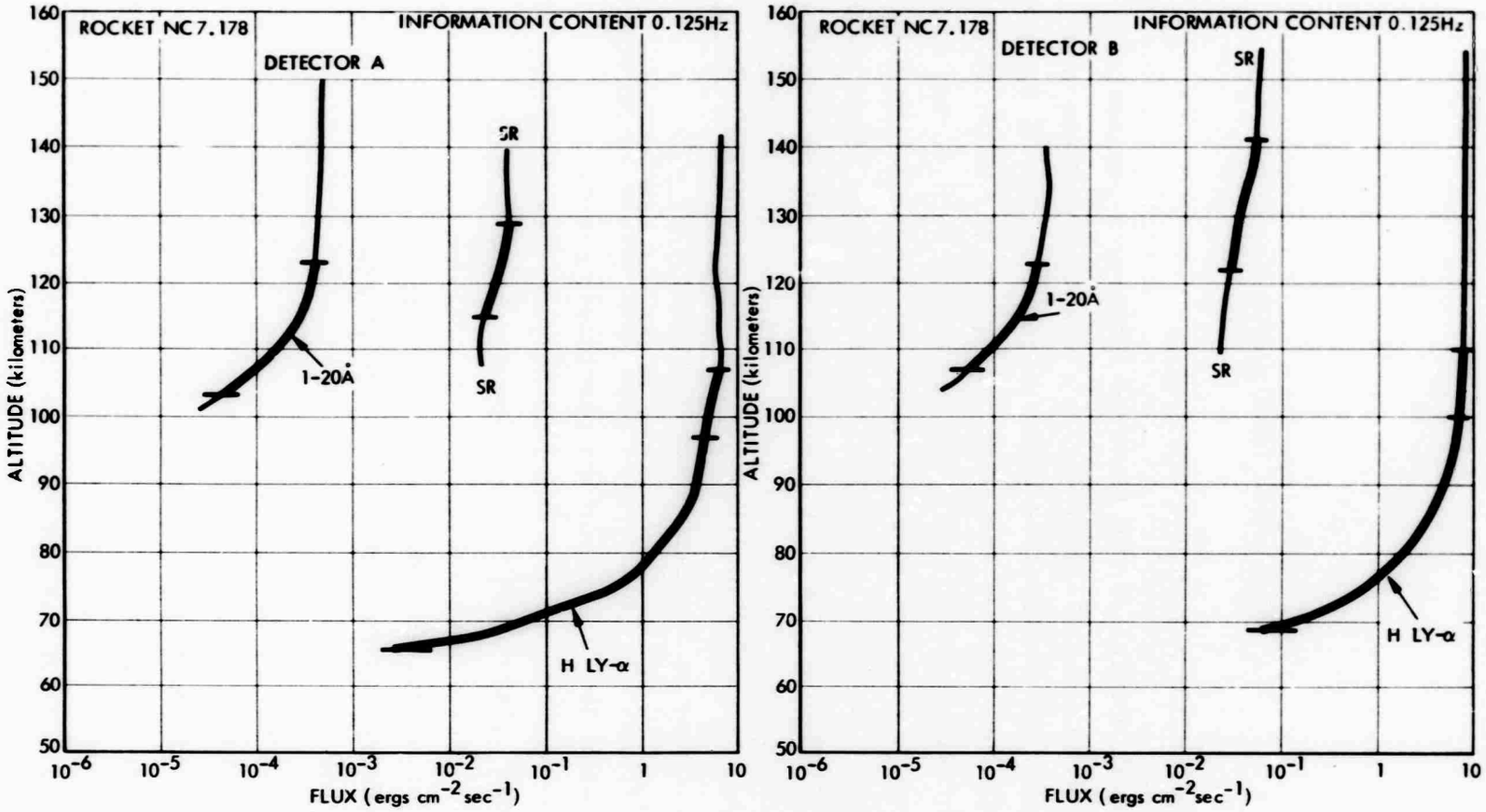

FIGURE 1. Solar Flux Versus Altitude - NC7.178 Rocket Vehicle Experiment

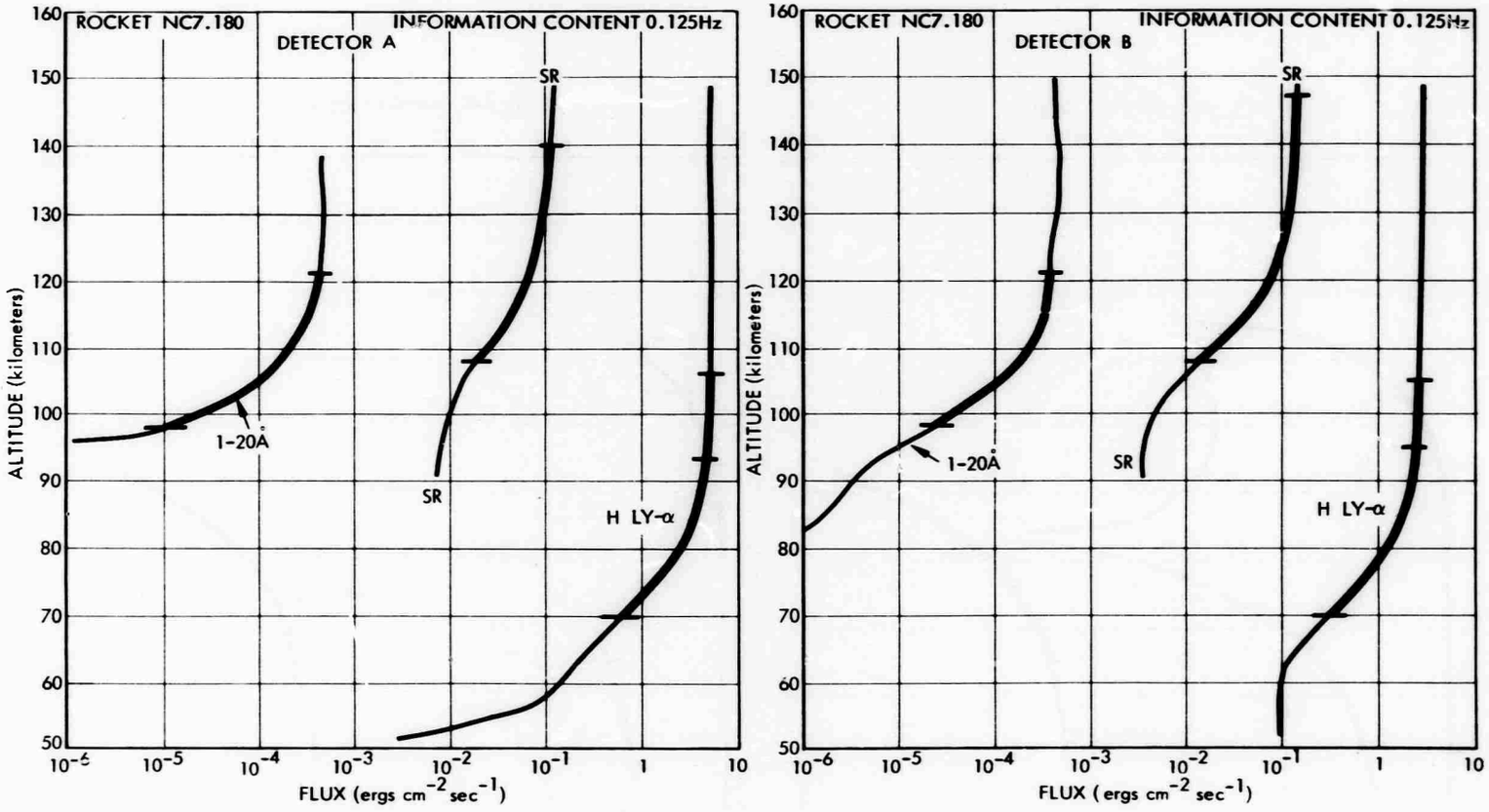

FIGURE 2. Solar Flux Versus Altitude - NC7.180 Rocket Vehicle Experiment

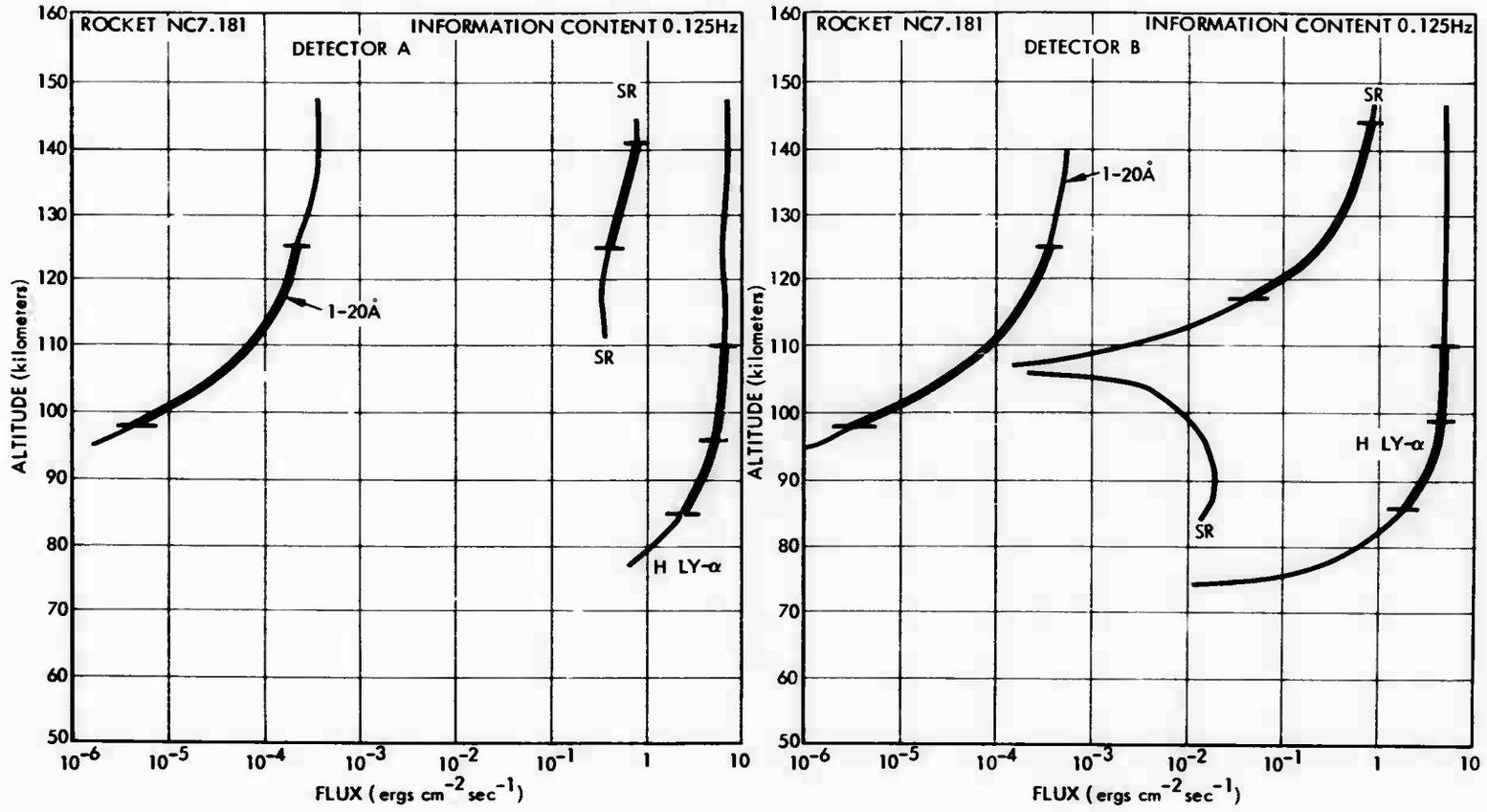

FIGURE 3. Solar Flux Versus Altitude - NC7.181 Rocket Vehicle Experiment

higher altitudes, an apparent bulge of O_2 density (as different from the density step) that is inconsistent with the determination of "total" particle density (i.e., sum of number densities of O_2 and N_2 and half the number density of O) occurs. This apparent bulge is reported by others (Lockey, Horton & Rofe, 1969). In the case of the present experiments it is believed to be the effect of absorption contamination of the H Ly-α line. This line penetrates deeply into the atmosphere because of its small absorption cross section (1×10^{-20} cm^2). Other radiation within the sensitivity band of the H Ly-α detector, e.g., the solar Si III line at 1206.5Å, may be the source of the contamination. The latter line, possessing perhaps 2 percent of the energy (Hinteregger, Hall & Schmidtke, 1964) of the H Ly-α line, has an absorption cross section 2000 times larger (Watanabe, 1958). Although solar energy of the 1206.5Å line disappears quickly as radiation penetrates the absorbing atmosphere, its effects perhaps contaminate measurements of the H Ly-α line by the H Ly-α detector.

Another example of explainable inconsistency in flux appears in the record of SR continuum flux measured by NC7.181 Channel 18 Detector B, shown in Fig. 3. In this record, the flux diminishes by absorption from its out-of-the-atmosphere value of 1 erg cm^{-2} sec^{-1} at about 150 km, to about 10^{-4} erg cm^{-2} sec^{-1} at about 106 km, and then increases as it penetrates to a local maximum of about $2(10^{-2})$ erg cm^{-2} sec^{-1} at approximately 90 km. This anomalous "negative absorption" is due to airglow-like re-emission of SR continuum radiation by a third-body recombination: atomic oxygen created by the H Ly-α produced dissociation of O_2 molecules recombines to form molecular oxygen. Similar re-emissions of SR continuum radiation at altitudes below about 100 km are apparent in the records of NC7.178 and NC7.180.

B. SOLAR FLUX OUTSIDE THE ABSORBING ATMOSPHERE

Solar flux intensities measured outside the absorbing atmosphere are given in Table 2. Measurements similar to NC7.178, 180, & 181 data in the 1-20Å wave band are given in Fig. 4. This figure

TABLE 2. FLUX INTENSITY OUTSIDE ATMOSPHERE ON 21 FEBRUARY 1966

BAND	WAVELENGTH (Å)	FLUX (ergs cm^{-2} sec^{-1})															
		AT ABOUT 1400 CST											AT 0710 CST				
		NC7.178 (Lat 60°N)				NC7.180 (Lat 30°N)				Of Lat 60°N & 30°N			NC7.181 (Lat 30°N)				
		A	B	SD	SD/M	A	B	SD	SD/M	MEAN	SD	SD/M	A	B	MEAN	SD	SD/M
Band dominated by Hydrogen Lyman-α (1215)	1140-1260	8.0	9.3	0.65	0.07	7.9	5.4	1.25	0.19	7.7	1.4	0.18	8.8	7.6	8.2	0.6	0.07
Schumann-Runge Continuum	1325-1475	0.073	0.078	0.002	0.026	0.10	0.17	0.035	0.25	0.105	0.038	0.36	0.88	0.98	0.93	0.05	0.054
1-20Å*	1-20	$7.1(10)^{-4}$	$7.5(10)^{-4}$	$0.2(10)^{-4}$	0.027	$6.9(10)^{-4}$	$6.8(10)^{-4}$	$0.05(10)^{-4}$	0.007	$7.1(10)^{-4}$ **	$0.3(10)^{-4}$	0.04	$6.1(10)^{-4}$	$7.5(10)^{-4}$	$6.8(10)^{-4}$ ***	$0.7(10)^{-4}$	0.10

* Taking solar source temperatures as $2(10)^6$ °K for 8Å < λ < 20Å and $4(10)^6$ °K for 1Å < λ < 8Å.

** X-Ray Monitoring Satellite (1965-93A, Explorer 30, NRL SOLRAD 8), measured $2(10)^{-3}$ ergs cm^{-2} sec^{-1} (McClinton and Kreplin, 1967).

*** X-Ray Monitoring Satellite (1965-93A, Explorer 30, NRL SOLRAD 8), measured $3(10)^{-3}$ ergs cm^{-2} sec^{-1} (McClinton and Kreplin, 1967).

A = Detector A

B = Detector B

SD = Standard deviation

M = Mean

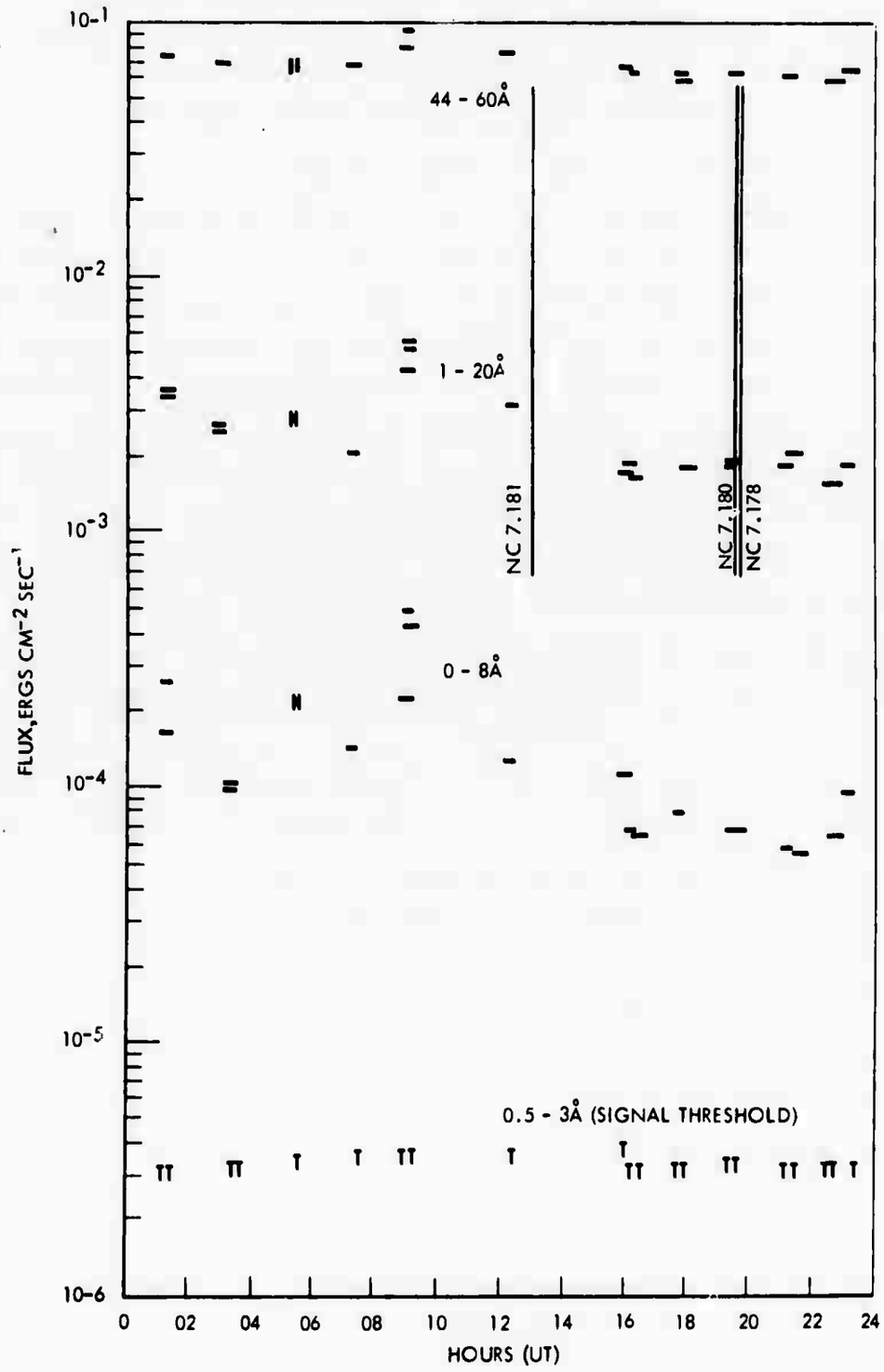

FIGURE 4. X-Ray Flux, Explorer 30 Satellite, 21 February 1966 (McClinton and Kreplin, 1967)

presents solar flux measured by an NRL X-ray monitoring satellite (1965-93A, Explorer 30, NRL SOLRAD 8) on the day the satellite was launched, which coincided with the launch date of NC7.178, 180, & 181.

Explorer 30 provided numerous measurements of solar X-ray emissions during 1966 (Kreplin, 1966) including those in the 1-8, 8-16, and 44-60Å wave bands. Fig. 4 shows a plot of X-ray flux versus time (UT) (McClinton & Kreplin, 1967) for these wave bands on which the 1-20Å measurement ranges of NC7.178, 180 & 181 are superimposed for time-of-measurement comparison. The ratio of 1-20Å to 0.8Å flux is 0.05 at NC7.181 launch time and 0.035 at NC7.178 and NC7.180 launch times. Flux was essentially constant between 1300 and 2000 GMT. This period includes the launch times of NC7.178, 180, and 181. Other data establishing solar emission constancy during the experimental period are given in Appendix A and by Grobecker (1967d).

NC7.178, 180, and 181 data provide measurements of 1-20Å flux that are comparable with those of Explorer 30 when computed for a sun temperature of 2×10^6 °K in this band. Computation of flux at a higher sun temperature (4×10^6 °K) makes for better consistency of density data at lower altitudes. Consequently, at the suggestion of Chubb (1970), flux in the 1-20Å band is computed as though it originated from two sources using a certain ratio of out-of-the-atmosphere emission intensities. This ratio is the relationship between intensities measured at the same time by Explorer 30 and given in Fig. 4, and intensities with emission temperatures of 2×10^6 °K in the 8-30Å band and of 4×10^6 °K in the 1-8Å band.

For another comparison of X-ray data, a plot prepared from data by Kreplin & Gregory (1963) of X-ray solar flux measurements by other experimenters is shown in Fig. 5. Observations of 2-8Å radiation intensity vary over 5 orders of magnitude in Fig. 5, and those of 0.5-3 and 1-20Å vary over nearly 3 orders of magnitude. Computation of these radiations, as being from a gray body source, are sensitive to the assumption of effective temperature of one or more sources in the sun.

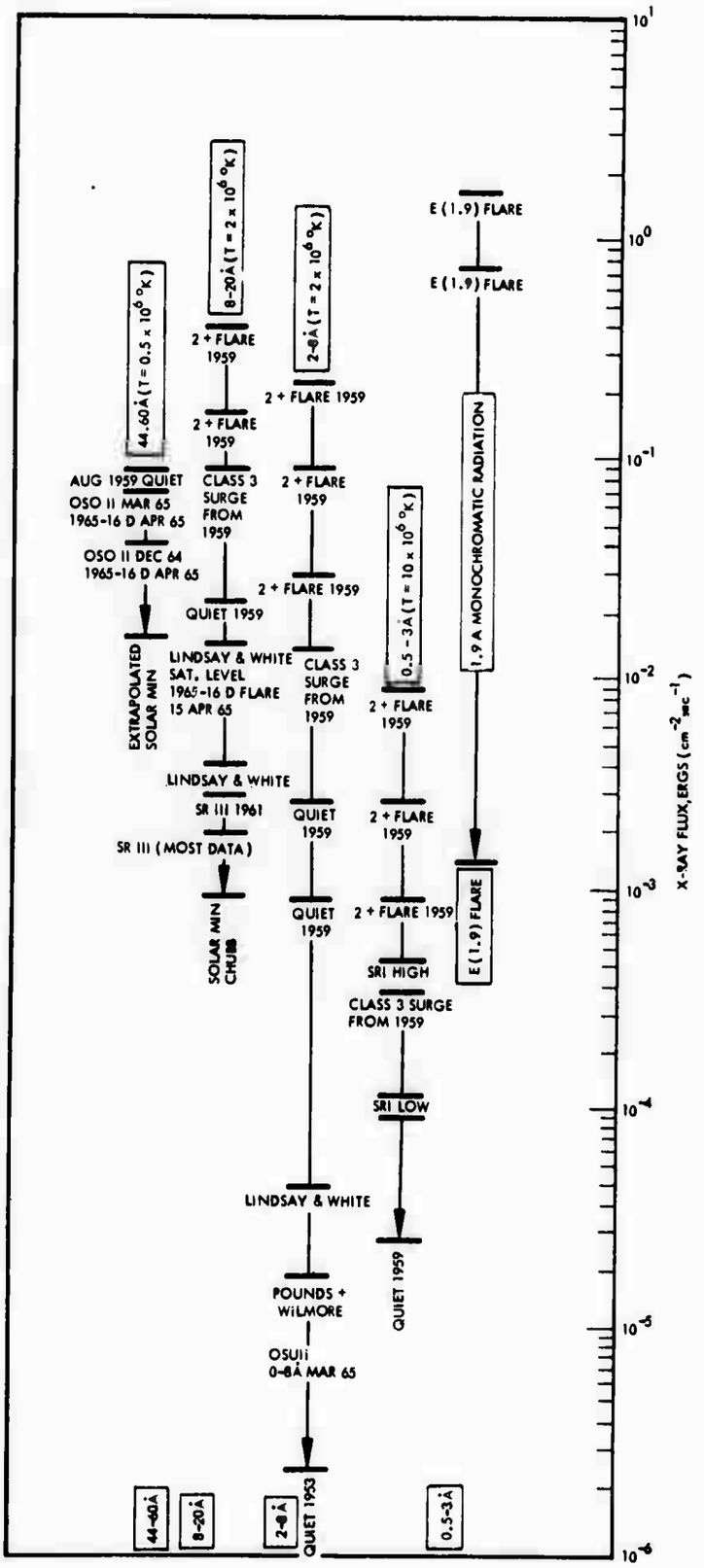

FIGURE 5. X-Ray Solar Flux Measurements of Various Experimenters (Kreplin & Gregory, 1963)

C. COMPUTATION OF SOLAR FLUX

Reduction of measurement data--an involved process accounting for laboratory calibrations of detectors and amplifiers and the effect of solar aspect angle with respect to detector axis--is described in detail elsewhere (Grobecker, 1967b, 1967c, and 1967e). Results of the measurements, expressed as detector current corrected to calibration conditions for sensitivity to normally directed flux, are summarized in the plots of Figs. 6, 7, and 8. Time is plotted against detector current (at an 8-cps rate) which is corrected for detector aperture function and solar aspect angle as measured in each of two detectors for each of the four range bands measured. Each plot point in Figs. 6 to 8 represents the mean of 20 or more points selected from continuously recorded data, digitized at about 400 cps. Since the 44-60Å flux determinations proved disappointingly sensitive to errors in determination of 1-20Å flux, the results from the 44-60Å detectors (as prepared for these experiments) are believed not useful for determining 44-60Å flux and are not discussed in the remainder of this report.

Corrected detector current data of Figs. 6, 7, and 8 are used in evaluating solar flux, measured by the three experiments, as a function of time. In the case of the 1-20Å wave band, the evaluation of solar flux involves the application of Eq. 1:

$$E_{(1\text{-}20\text{Å})}(z_1) = \frac{I_{(1\text{-}30\text{Å})}(z_1)}{q_{eff}\,\sigma_G\,T_{3f}} \cdot \frac{\int_{1\text{Å}}^{8\text{Å}} \left\{ e^{\tau}\left[-\sigma(\lambda)N(z_1)\right] d\lambda \Big/ \lambda^5 \left[e^{\tau}(hc/\lambda T_8)-1\right]\right\} + \int_{8\text{Å}}^{20\text{Å}} \left\{ e^{\tau}\left[-\sigma(\lambda)N(z_1)\right] d\lambda \Big/ \lambda^5 \left[e^{\tau}(hc/\lambda T_{30})-1\right]\right\}}{\int_{1\text{Å}}^{8\text{Å}} \left\{ \epsilon(\lambda)\, e^{\tau}\left[-\sigma(\lambda)N(z_1)\right] d\lambda \Big/ \lambda^5 \left[e^{\tau}(hc/\lambda T_8)-1\right]\right\} + \int_{8\text{Å}}^{30\text{Å}} \left\{ \epsilon(\lambda)\, e^{\tau}\left[-\sigma(\lambda)N(z_1)\right] d\lambda \Big/ \lambda^5 \left[e^{\tau}(hc/\lambda T_{30})-1\right]\right\}} \tag{1}$$

where I = ion chamber current due to radiation in 1-30Å band.

T_8 = temperature of solar source of 1-8Å radiation = $4 \times 10^6\ ^oK$

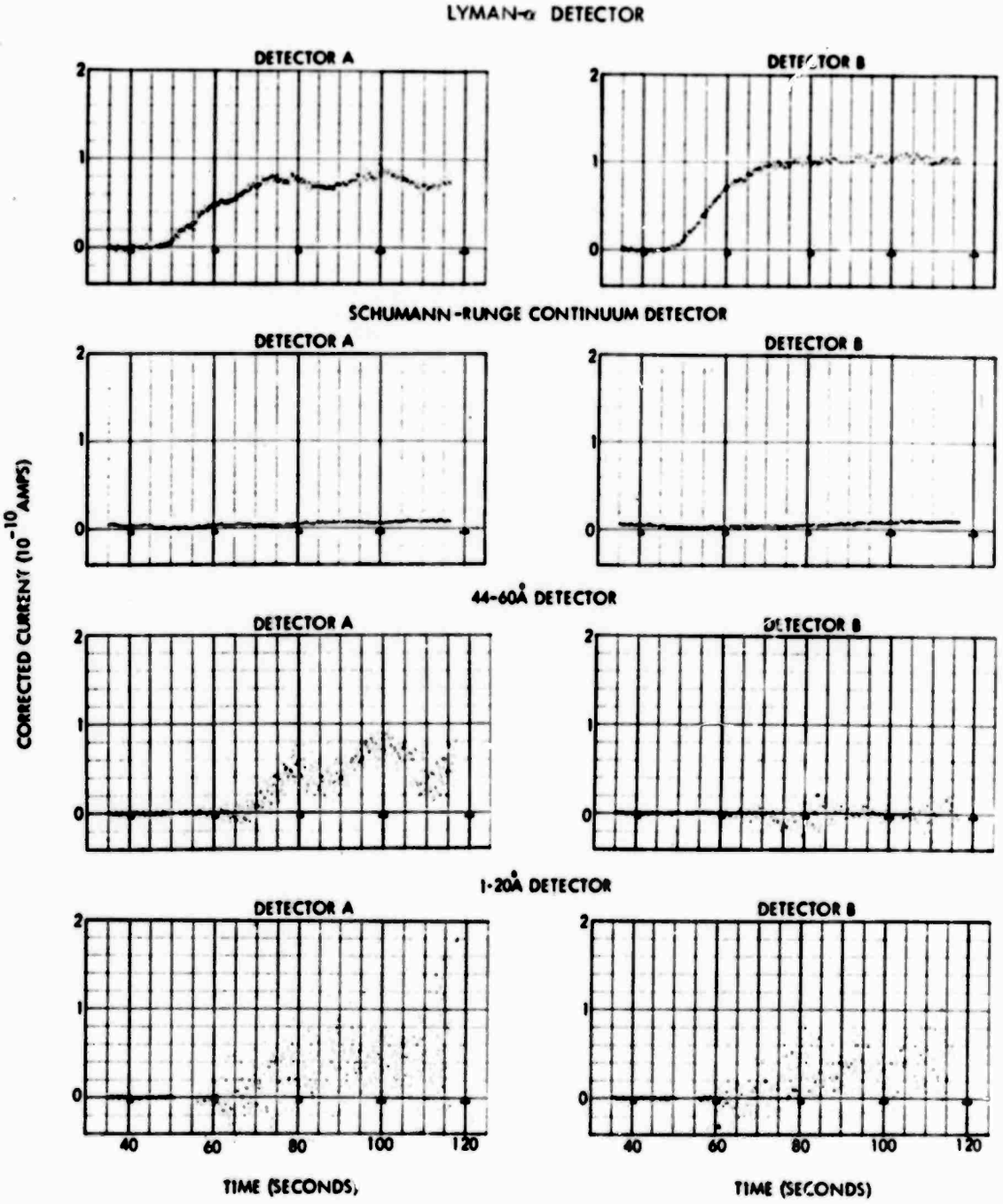

FIGURE 6. Detector Current Versus Time - NC7.178

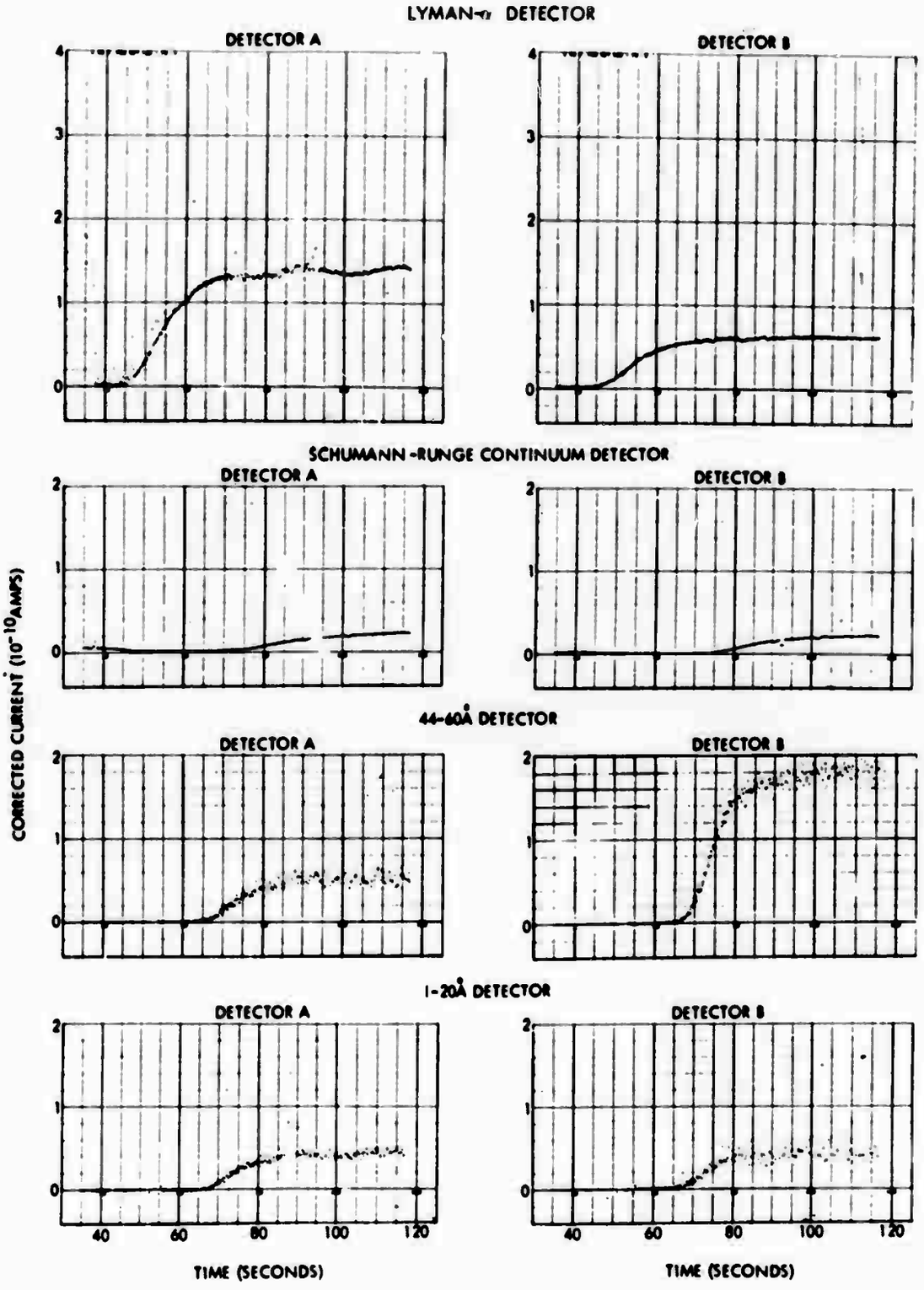

FIGURE 7. Detector Current Versus Time - NC7.180

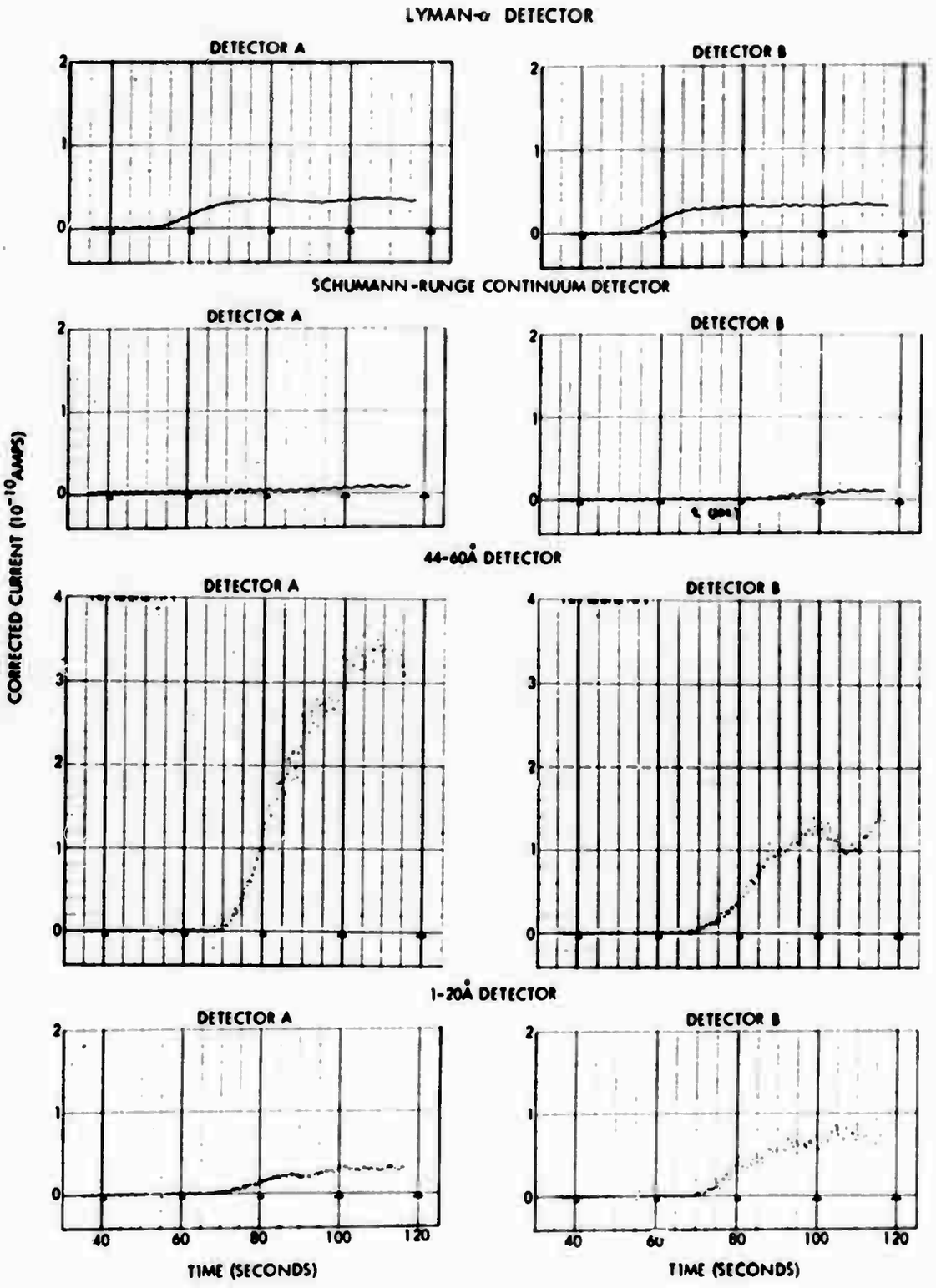

FIGURE 8. Detector Current Versus Time - NC7.181

T_{30} = temperature of solar source of 8-30Å radiation = 2×10^6 °K

$\epsilon(\lambda)$ = efficiency of "1-20Å detector" of normalized spectral shape given in Fig. 9 and value at 8Å given in Table 3.

q = charge on the electron

c = 1.43879 cm °K

w = $5.4(10)^{10}$ ion pairs per erg based on ionization potential 11.47V for filling gas CCl_4

a = area of detector aperture as given in Table 3.

G_G = gas gain, as given in Table 3.

G_{ap} = gain reduction due to aperture restriction, as given in Table 3.

$\sigma(\lambda) = 0.22\sigma_{O_2}(\lambda) + 0.78\sigma_{N_2}(\lambda)$, determined from values given in Fig. 10.

$N(z_i) = \int_{z_i}^{\infty} F(z_i)n(z_i)dz_i$ - overhead air mass, above altitude z_i; based on U.S. Standard Atmosphere, 1962.

$F(z_i)$ = Optical depth factor given in Table 4.

K = $E(1\text{-}8Å)(z_i)/E(8\text{-}30Å)(z_i)$, ratio of flux in 1-8Å and 8-30Å bands as determined from measurements of Explorer 30 satellite, given in Fig. 4.

Evaluation of solar flux in the SR continuum involves the application of a relation similar to that of Eq. 1, except the solar source is taken to be single and at a temperature of 4800 °K. The spectra of detector efficiency for the detectors of the SR continuum are given in Fig. 11.

H Ly-α flux is evaluated in terms of ion chamber current by:

$$I = qwa\epsilon E \qquad (2)$$

where I = ion chamber current

ϵ = photon detection efficiency at H Ly-α

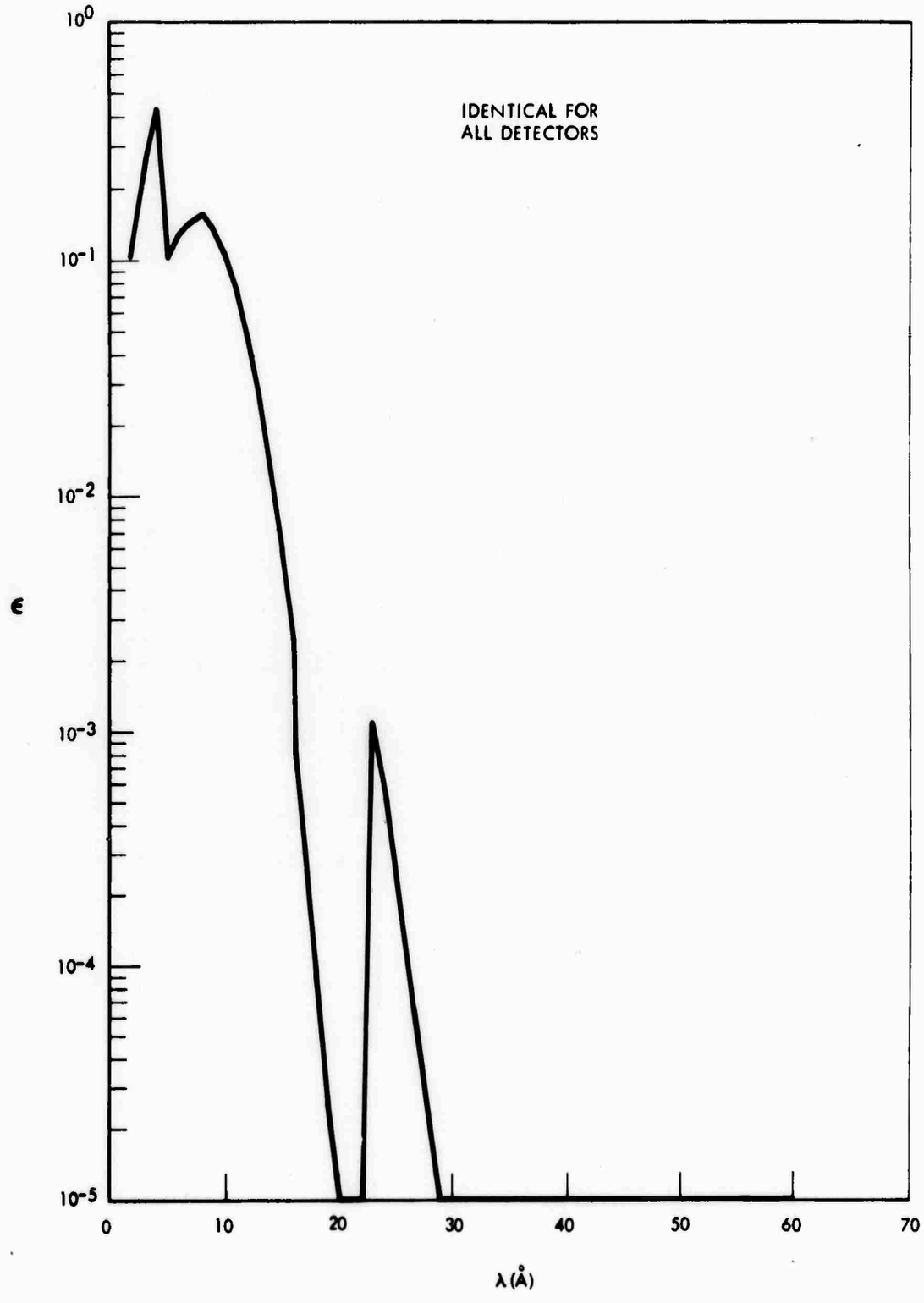

FIGURE 9. Spectrum of Photon Efficiency - 1-20Å Detectors, Channel 14

TABLE 3. EXPERIMENT INSTALLATION PARAMETERS

Rocket No.	Channel No. (IRIC)	Detector Identification No.	Band Å	Aspect Phase	Look Angle (deg)	Negative Shell (volts)	Gas Gain (G_G)	Aperture Diameter (in.)	Aperture Gain (G_{ap})	Window				Filling Gas		Calibration Efficiency		
										Material	W_x (cm)	W_D (gm cm^{-1})	Area a (cm^2)	G_x (cm)	α (pairs/erg)	ϵ_{1216}	ϵ_{1375}	ϵ_8
NC7.178	14	M1701 M1606	8-20	A B	90 70	1102	45.0 54.0	0.750 0.750	1.0 1.0	$C_{10}H_8O_4$ Al CCl_4 (27-mm Hg)	0.000625 $1.5\ (10)^{-5}$ 0.2185	1.35 2.699 $1.32\ (10)^{-4}$	2.85	2.32	$5.47\ (10)^{10}$			0.224 0.215
	15	M598 M597	Lyman-α	A B	90 70	20	1.0 1.0	0.043 0.043	0.013 0.013	LiF	See empirical calibration		0.78		$8.13\ (10)^{10}$	0.1356 0.1384		
	17	M1708 M1609	44-60	A B	90 70	1949	132.0 24.0	0.206 0.206	0.076 0.076	$C_{10}H_8O_4$ Cr CO_2 (94-mm Hg) N_2	0.000625 $6.0\ (10)^{-7}$ 0.2185 0.2185	1.35 8.0 $2.45\ (10)^{-4}$ $3.98\ (10)^{-4}$	2.85	2.32	$4.55\ (10)^{10}$			0.125 0.125
	18	M1499 M1697	Schumann-Runge	A B	90 70	20	1.0 1.0	0.375 0.375	1.0 1.0	BaF_2	See empirical calibration		0.78		$6.93\ (10)^{10}$		0.0616 0.0638	
NC7.180	14	M1583 M1576	8-20	A B	65 45	1107	51.0 57.0	0.750 0.750	1.0 1.0	$C_{10}H_8O_4$ Al CCl_4 (27-mm Hg)	0.000625 $1.5\ (10)^{-5}$ 0.2185	 $1.32\ (10)^{-4}$	2.85	2.32	$5.47\ (10)^{10}$			0.216 0.181
	15	M1482 M1483	Lyman-α	A B	65 45	20	1.0 1.0	0.054 0.054	0.0206 0.0206	LiF	See empirical calibration		0.78		$8.13\ (10)^{10}$	0.1674 0.1385		
	17	L1416 L1420	44-60	A B	65 45	1441	235.0 220.0	0.375 0.375	0.25 0.25	$C_{10}H_8O_4$ Cr CO_2 N_2	0.000625 $6.0\ (10)^{-7}$ 0.2185 0.2185	1.35 8.0 $2.45\ (10)^{-4}$ A-$3.42\ (10)^{-4}$ B-$4.55\ (10)^{-4}$	2.85	2.32	$4.55\ (10)^{10}$			0.136 0.113
	18	M1495 M1498	Schumann-Runge	A B	65 45	20	1.0 1.0	0.375 0.375	1.0 1.0	BaF_2	See empirical calibration		0.78		$6.93\ (10)^{10}$		0.0675 0.0556	
NC7.181	14	M1607 M1571	8-20	A B	90 70	1142	40.0 69.0	0.750 0.750	1.0 1.0	$C_{10}H_8O_4$ Al CCl_4 (27-mm Hg)	0.000625 $1.5\ (10)^{-5}$ 0.2185	 $1.32\ (10)^{-4}$	2.85	2.32	$5.47\ (10)^{10}$			0.234 0.225
	15	M1480 M1479	Lyman-α	A B	90 70	20	1.0 1.0	0.0316 0.0316	0.0071 0.0071	LiF	See empirical calibration		0.78		$8.13\ (10)^{10}$	0.0995 0.1183		
	17	L1423 L1406	44-60	A B	90 70	1404	225.0 153.0	0.437 0.437	0.34 0.34	$C_{10}H_8O_4$ Cr CO_2 A-103-mm Hg B-79-mm Hg N_2	0.000625 $6.0\ (10)^{-7}$ 0.2185 0.2185	 A-$2.69\ (10)^{-4}$ B-$2.06\ (10)^{-4}$ A-$4.59\ (10)^{-4}$ B-$4.31\ (10)^{-4}$	2.85	2.32	$4.55\ (10)^{10}$			0.113 0.136
	18	M1491 M1490	Schumann-Runge	A B	90 70	20	1.0 1.0	0.100 0.100	0.071 0.071	BaF_2	See empirical calibration		0.78		$6.93\ (10)^{10}$		0.0544 0.0600	

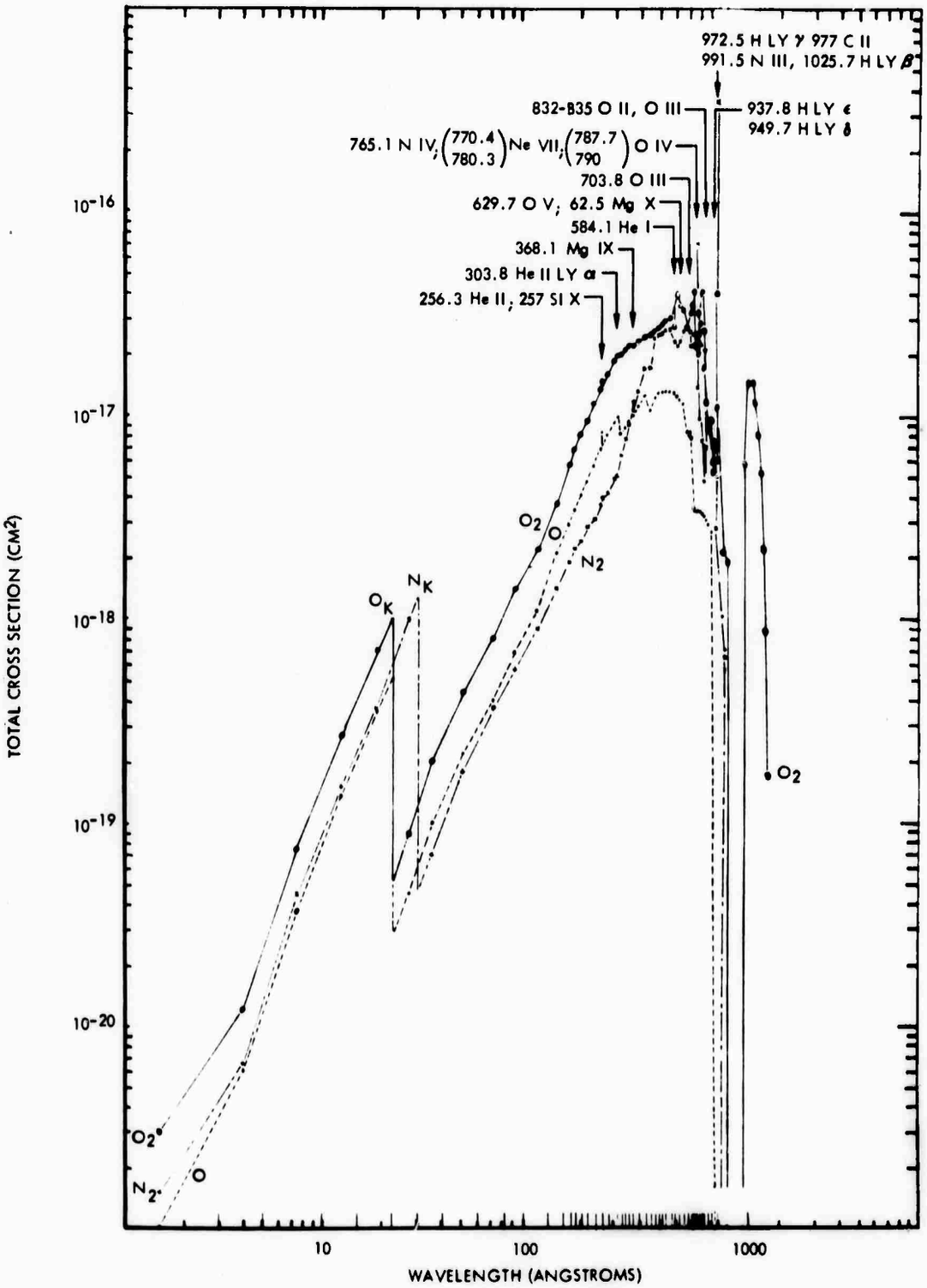

FIGURE 10. Absorption Cross Section of O, O_2, and N_2 (after tabulated data of Hinteregger et al., 1964)

TABLE 4. OPTICAL DEPTH FACTORS

Height above Sea Level (z) (km)	Molecular Weight ($gm\ mole^{-1}$)	Temperature (^{o}K)	Scale Height (H) (km)	$\beta = \frac{dH}{dz}$	$X = \left(\frac{6367+z}{H}\right)$	$F\left(\frac{6367+z}{H}, X\right)$ NC7.178	$F = \sec X$ NC7.180	$F\left(\frac{6367+z}{H}, X\right)$ NC7.181
				-0.027				
50	28.97	270.8	8.06	-0.051	800	3.38	1.531	6.11
60	28.97	252.8	7.55	-0.098	850	3.38	1.532	6.12
70	28.97	218.0	6.53	-0.037	980	3.38	1.533	6.16
80	28.97	205.0	6.16	+0 038	1040	3.38	1.534	6.17
90	27.52	206.2	6.54	+0.072	980	3.38	1.535	6.16
100	26.22	217.3	7.26	+0.093	900	3.38	1.535	6.14
110	25.03	233.3	8.19	+0.185	790	3.37	1.536	6.13
120	23.95	272.8	10.04	+0.186	625	3.36	1.537	6.04
130	22.50	302.9	11.90	+0.178	540	3.35	1.537	5.9
140	21.21	327.3	13.68	+0.176	475	3.34	1.538	5.87
150	20.06	348.4	15.44	+0.180	420	3.33	1.539	5.82
160	19.34	368.0	17.24	+0.187	380	3.32	1.540	5.79
170	18.10	386.7	19.11	+0.186	340	3.31	1.542	5.78
180	17.26	403.4	20.97	+0.187	315	3.30	1.544	5.73
190	16.50	418.5	22.84					

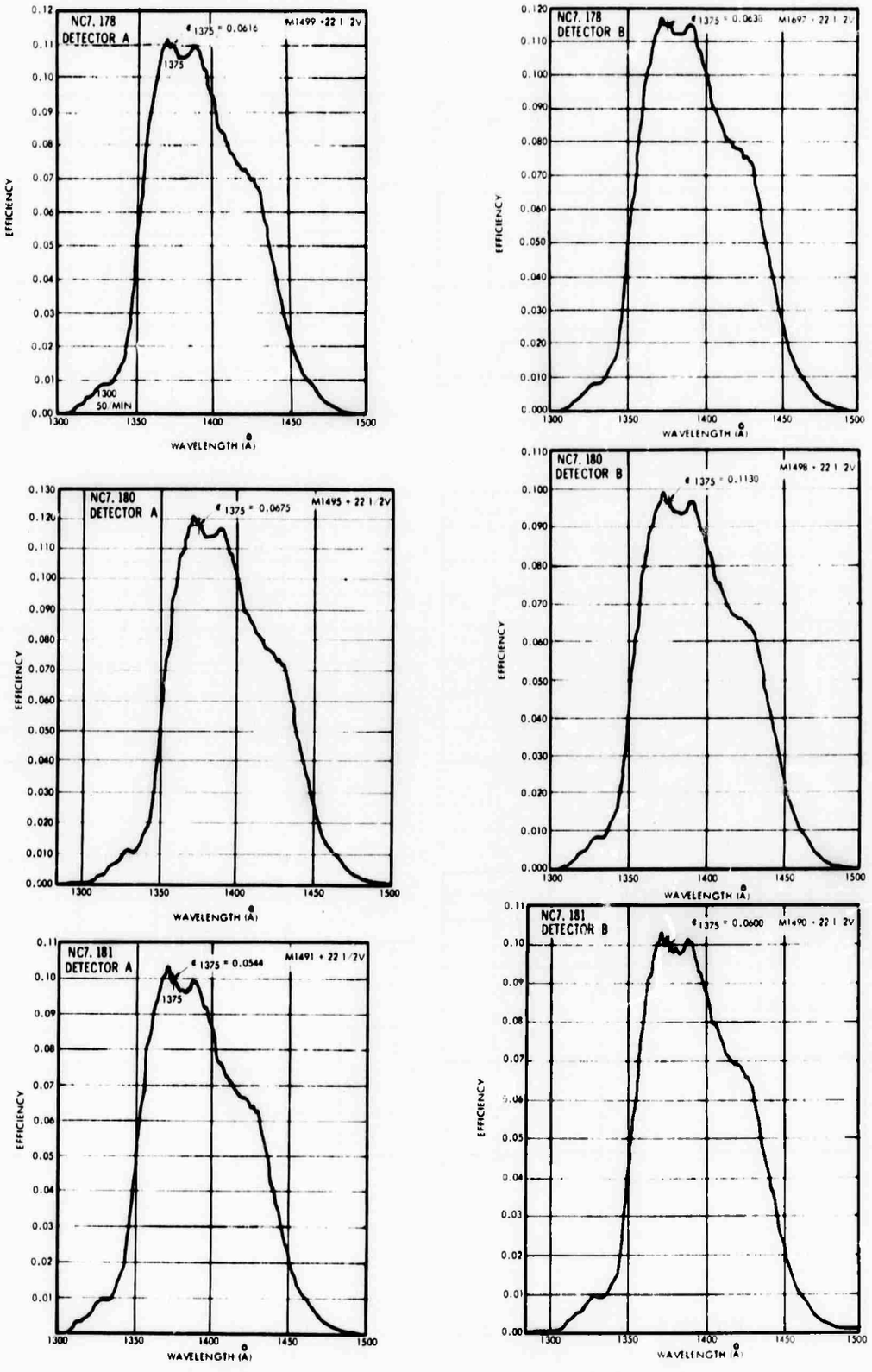

FIGURE 11. Spectra of Efficiency - SR Detector

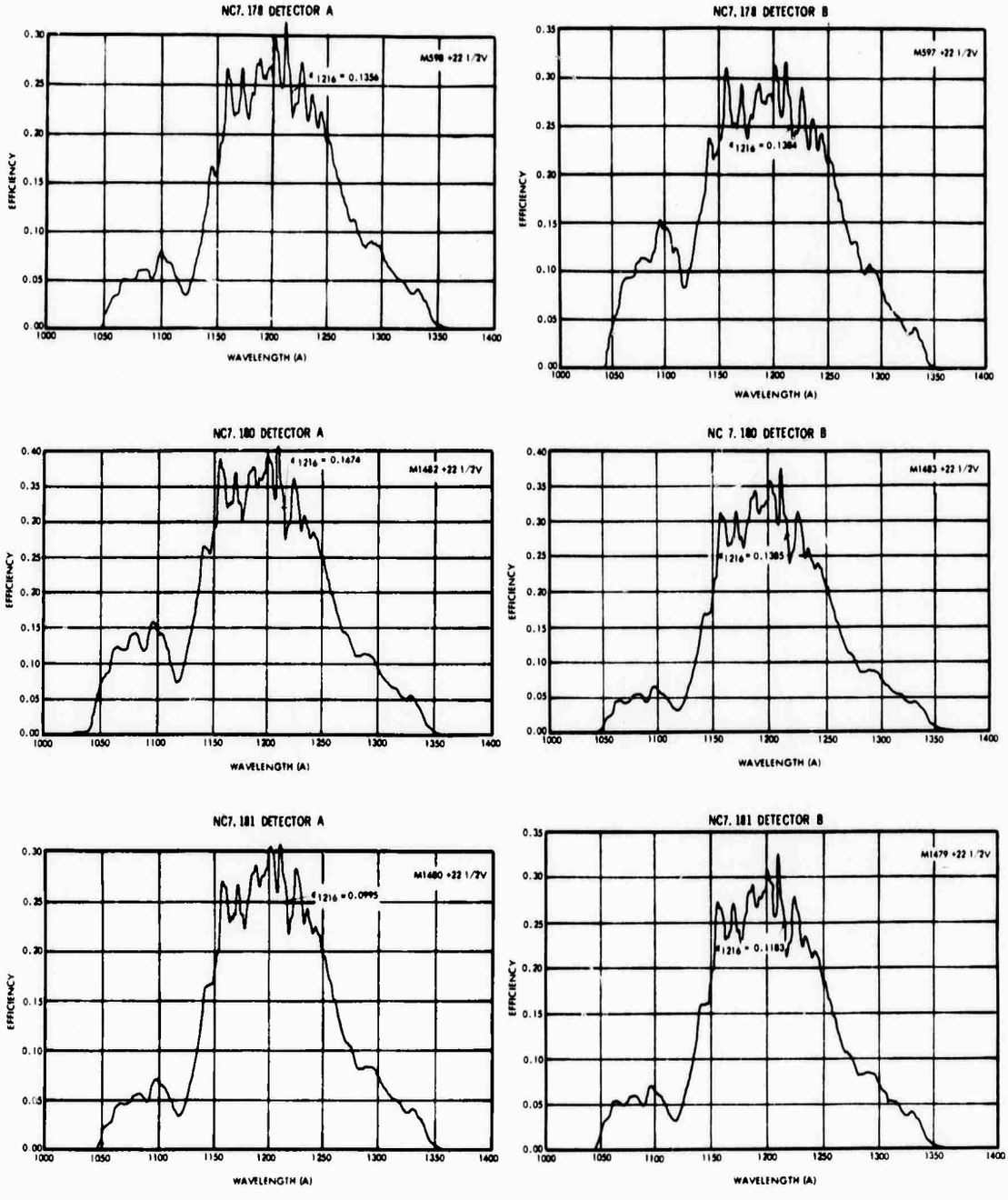

FIGURE 12. Spectra of Efficiency - H Ly-α Detector

E = energy flux in Lyman-α line

w = ion pairs per erg, assumed to be one per photon

a = window area, accounting for aperture restrictions

q = electron charge.

The spectrum of detection efficiency of the H Ly-α detectors is given in Fig. 12.

These computations yield data of point frequency about 8 cps, which are noisy and require smoothing. The data were smoothed by a sequence of filtering operations: frequencies of the measurement spectrum expected to be artifacts of the instrumentation are eliminated, and frequencies expected to be characteristic of the geophysical variation are left intact.

The progressive elimination of unwanted frequencies from the data is illustrated in the frequency chart of Fig. 13. The maximum frequency content of the original measurement data is about 200 cps, corresponding to the approximate 5 ms rise time of the detector. On this basis, the continuous record of telemetered data is digitized at 400 cps to ensure that all frequencies contained in the instrument signal are contained in the digitized data.

Spectral analysis of the digitized data, of which Fig. 14 is an out-of-the-atmosphere example, shows that frequency power greater than 50 cps in the measurement data is negligible. Spectral analyses of data sections from each rocket digitized at 800 cps showed no additional lines. It is believed that no "aliasing" frequencies exist in the spectrum of data digitized at 400 cps.

Frequencies near 50 cps, shown in Fig. 14 and schematically in Fig. 13, are harmonics ascribed to irregularities in the ion-chamber aperture function. This function describes the reduced sensitivity of the detector to radiation incident at angles other than the normal incidence ones of laboratory calibrations, and its variations depend on detector geometry and composition, which must be accounted for (Grobecker, 1967e).

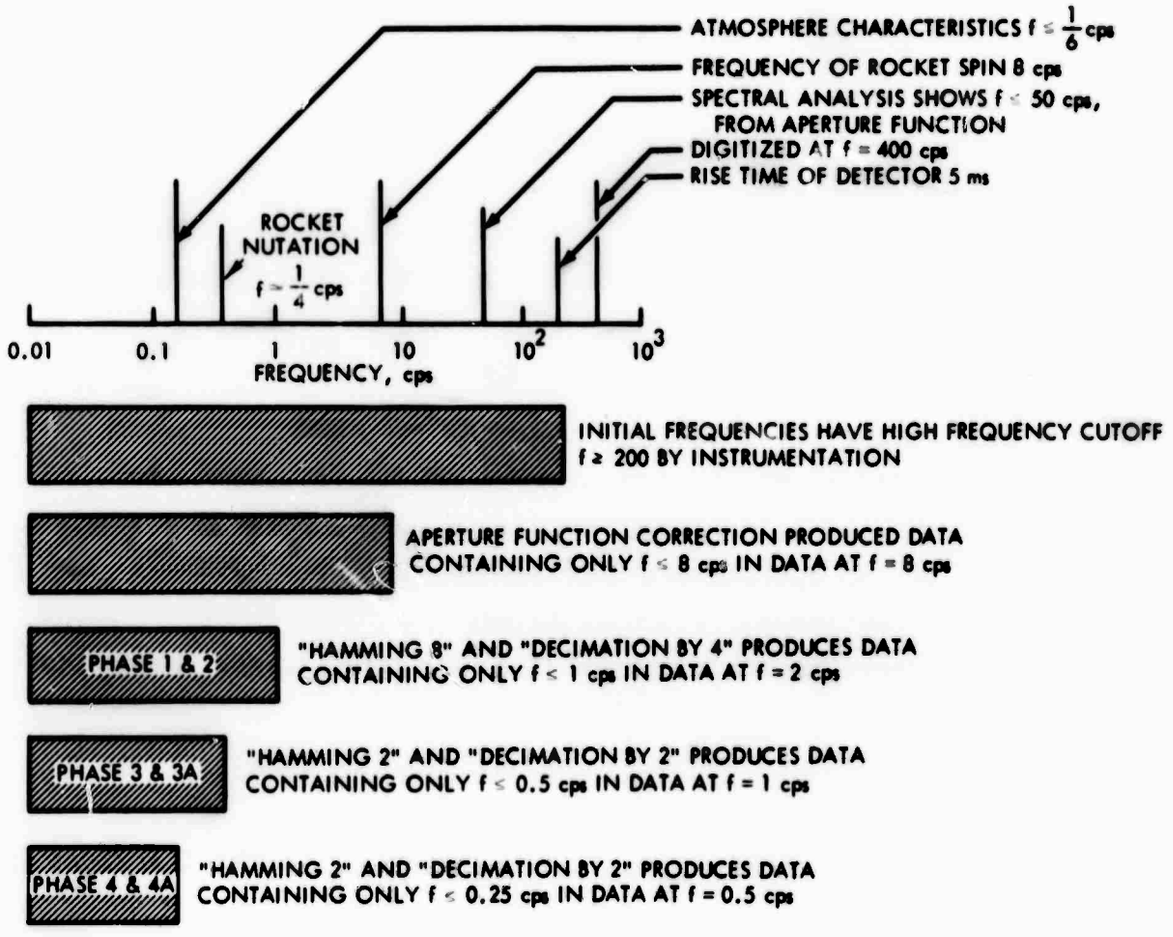

FIGURE 13. Smoothing of Solar Flux E(t)

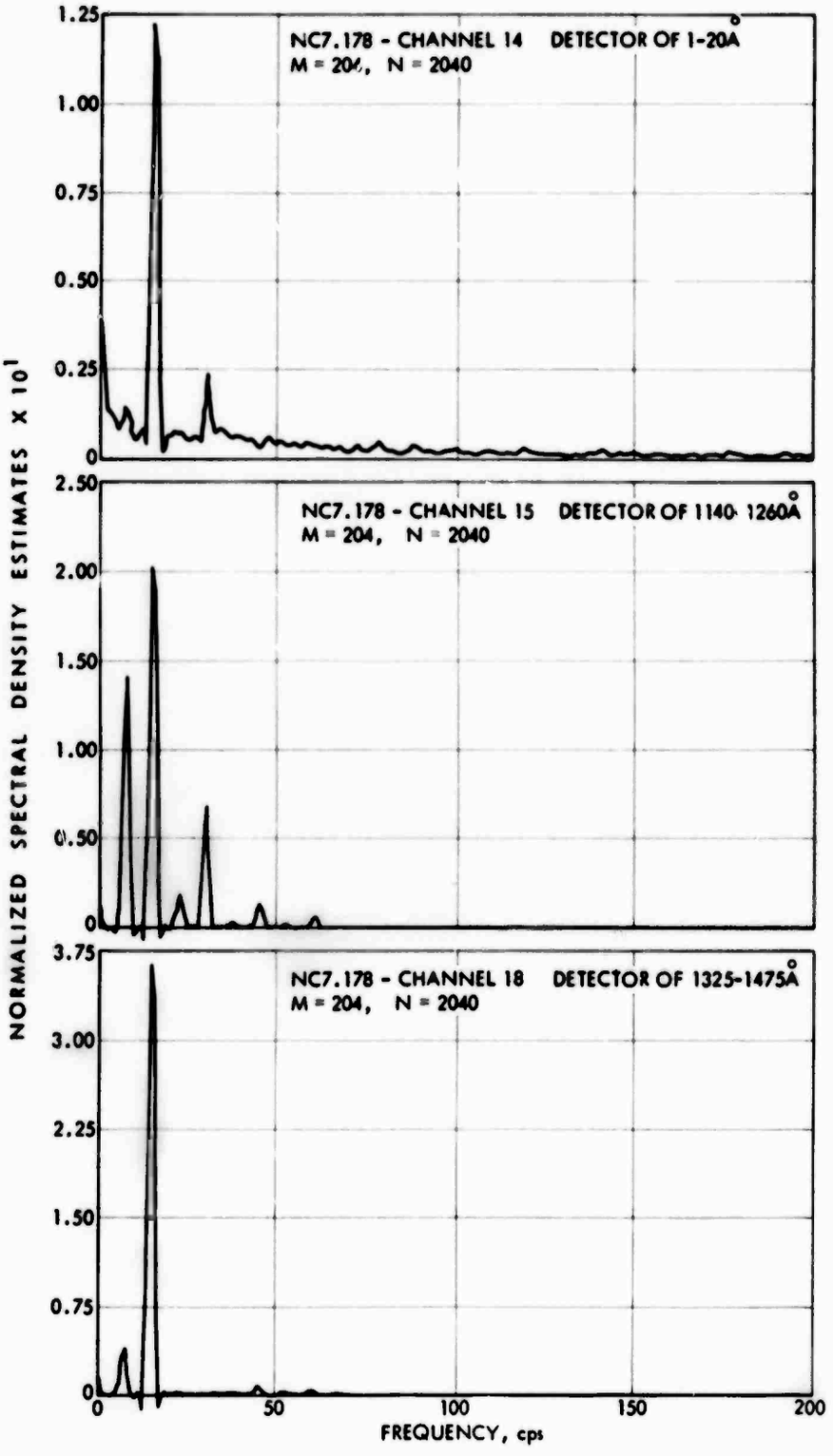

FIGURE 14. Spectral Analyses of Digitized Data of Rocket NC7.178

The frequency of the rocket spin at about 8 cps and its second harmonic appear as a strong modulation of the measurement data. A slow modulation, due to precession of the rocket and causing yaw angle with respect to the trajectory, is superimposed on the 8 cps. This precession has a period of more than 20 sec. In addition to the precession, nutation of the rocket (giving small yawing motion) is characterized by a frequency of $\frac{1}{3}$ to $\frac{1}{4}$ cps. Considering the speed with which the rocket moves through the atmosphere, and that the expected atmospheric changes are to be sensed in vertical intervals approximated by atmospheric scale heights, the investigated atmospheric characteristics are expected to involve frequencies smaller than about $\frac{1}{6}$ cps.

To selectively filter out the several unwanted frequencies that are artifacts of instrumentation (schematically shown in Fig. 13), filters described by Blackman and Tukey (1958) were employed in a succession of computing operations. These are the "hamming" filters D_{38} (where $m = 8$) and D_{32} (where $m = 2$). The D_{38} filter converted 320 points of data, with content in the 0- to 8-cps range, to 320 points of data with information content of less than 1 cps frequency. Filter D_{32} converted 80 points of data with content from 0-1 cps to 80 points with information content of frequency less than 0.5 cps. Following each hamming, a "decimation" by 4 to 2 cut down the number of data points. If done properly, decimation does not introduce aliased frequencies into the information content of the reduced band.

Frequency transmission characteristics of filters D_{38} and D_{32}, as applied to 8 cps data and 1 cps data, respectively, are shown in Fig. 15. As evidenced by the Fourier transforms, the content remaining after hamming is trivial at frequencies higher than the cut-off frequency.

An N point hamming filter is defined as follows: if

$$x_j \text{ transforms by hamming to } x_j^* \ (j = 1,\ldots,m),$$

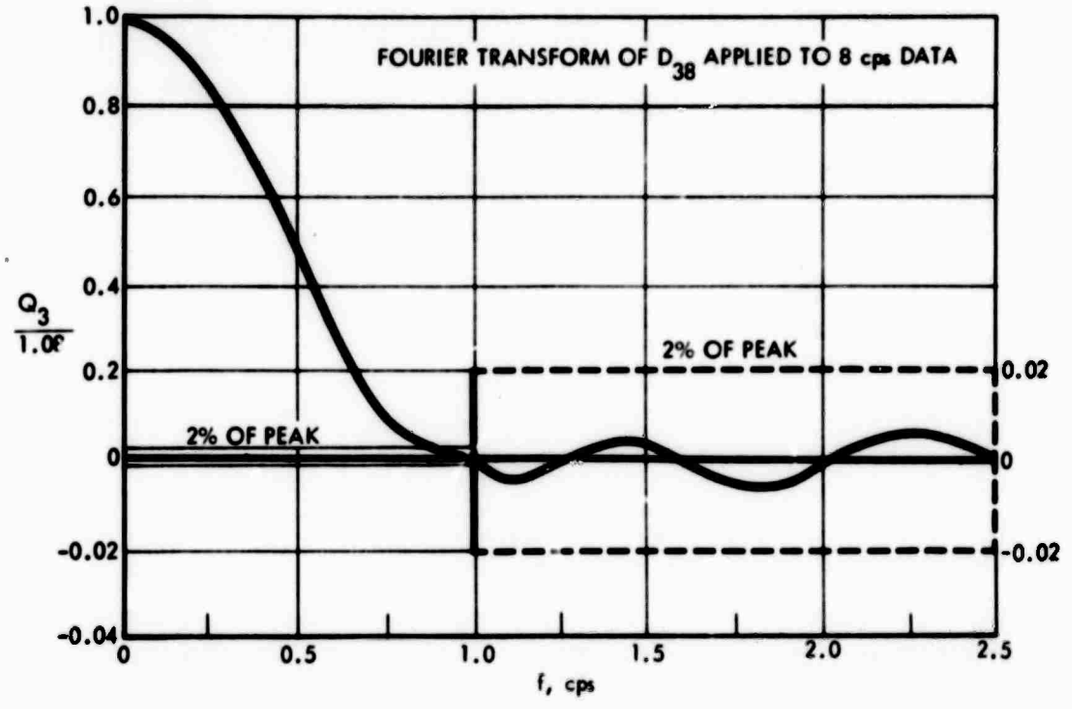

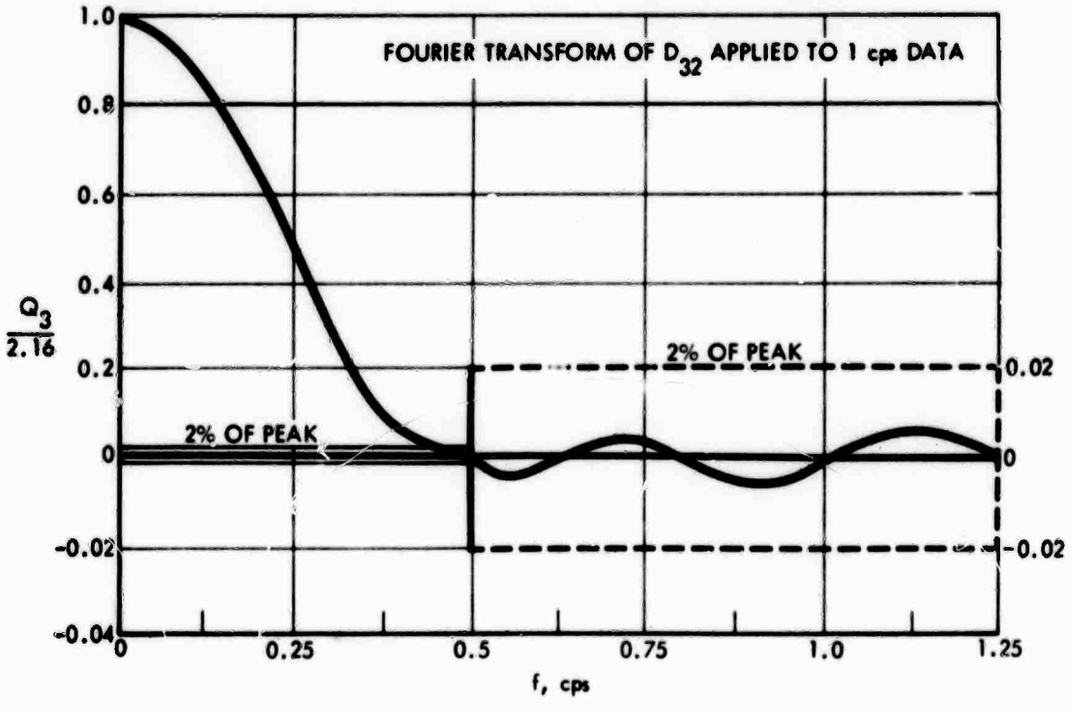

FIGURE 15. Fourier Transforms of Filters D_{38} and D_{32}

then $D_t = 0.54 + 0.46 \times \cos \frac{\pi t}{N}$ $(t = -N, N)$ and $W = \sum_{t=-N}^{N} D_t$;

accordingly $x_j^* = x_j$ $(j = 1,\ldots,N)$ and is defined by:

$$x_j^* = \sum_{t=-N}^{N} x_{j-t} D_t / W \quad (j = N + 1,\ldots,m - N)$$

$$x_j^* = x_j \quad (j = m - N + t,\ldots,m) \; . \tag{3}$$

A decimation by N takes every N^{th} point:

x_j transforms by decimation to x_t^* $\left(t = 1,\ldots,\frac{m}{N} \; ; \quad j = 1,\ldots,m\right)$

and $x_t^* = x_{1 + (t - 1)N}$ $\left(t = 1,\ldots,\frac{m}{N}\right)$. (4)

A hamming-N operation changes the information content by $\frac{1}{N}$, and a decimation by N changes the data frequency by $\frac{1}{N}$. Table 5 describes the effects of the successive filtering process applied to the original 8 cps data.

In summary, the filtering procedure applied to the experimental data was sequenced as follows:

1. Hamming-8 filter reduced the data frequency content from more than 1 cps to less than 1 cps
2. Decimation by 4 reduced the number of data points to be handled from 8 to 2 cps
3. Hamming-2 filter reduced the data content to frequencies less than 0.5 cps
4. Decimation by 2 reduced the 2 cps data to less than 1 cps.

TABLE 5. EFFECTS OF SUCCESSIVE FILTERING AND DECIMATION OPERATIONS IN SMOOTHING FLUX DATA [E(t)]

Filter Operation		Data Frequency (cps)	Maximum (cps) Information Content
Hamming-8	H_8	8	1
Decimation by 2	D_4	2	1
Hamming-2	H_2	2	0.5
Decimation by 2	D_2	1	0.5
Hamming-2	H_2	1	0.25
Decimation by 2	D_2	0.5	0.25
Hamming-2	H_2	0.5	0.125
Decimation by 2	D_2	0.25	0.125
Hamming-2	H_2	0.25	0.062

Final data, whose frequency content was less than 0.125 cps in a data frequency of 0.5 cps, were produced by second and third applications of steps 3 and 4.

An example of the data without filtering or decimations, digitized at 8 cps and describing information of frequencies up to 4 cps, is given in Fig. 16. These data, after hamming and decimation, are shown in Fig. 17 where information content is less than 0.125 cps at a 0.5 cps data rate. Further iterations of hamming and decimation, which go too far by reducing information content to frequencies less than 0.062 in data points of 0.25 cps, yielded results shown in Fig. 18.

After reviewing the results of successive filtering applications to all data, the flux data of all channels were reduced to data points at a frequency of 0.5 cps, retaining information smoothed to contain only frequencies less than 0.125 cps.

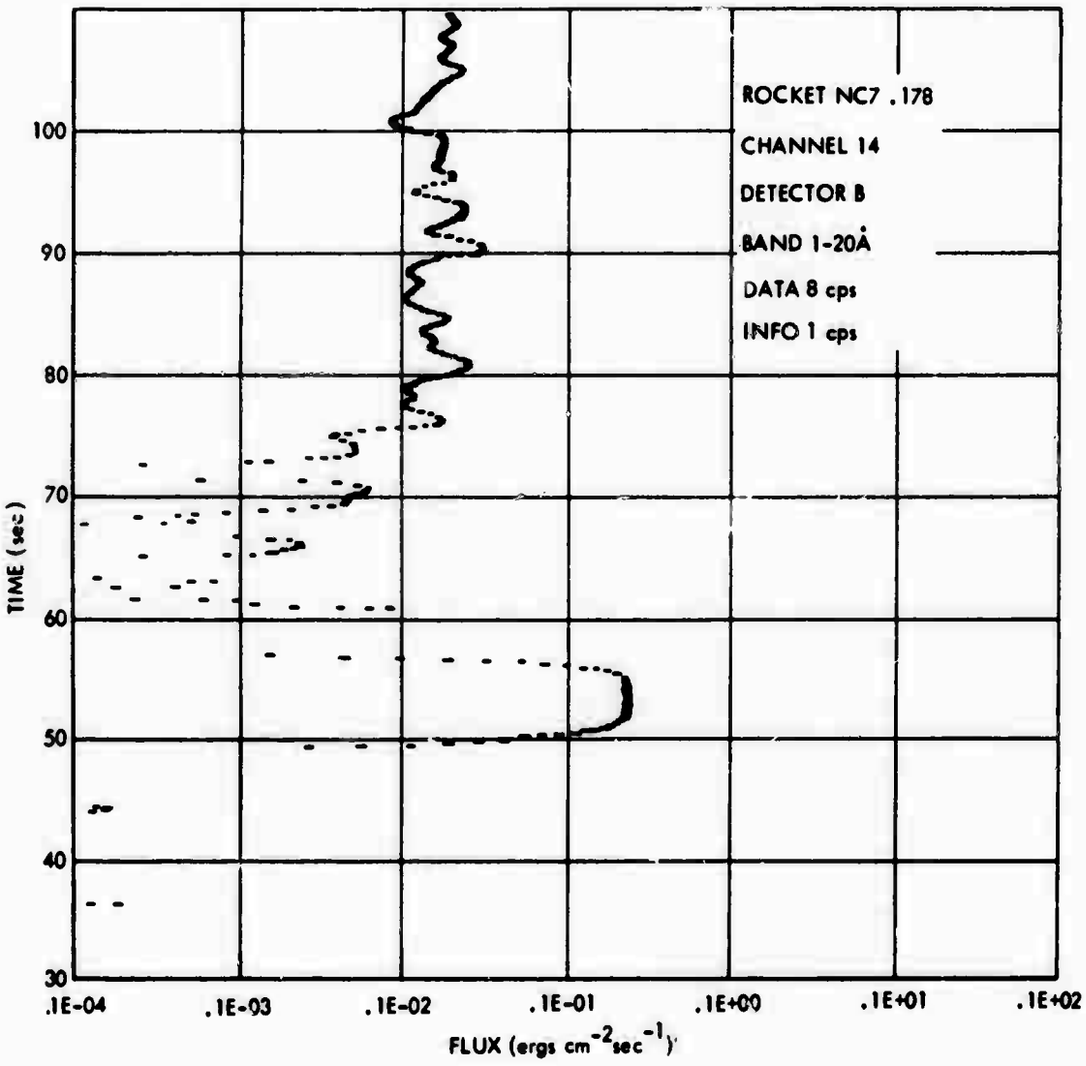

FIGURE 16. Flux Versus Time at Data Frequency 8 cps and Information Content 1 cps - 1-20Å Band, NC7.178 Detector B, Channel 14

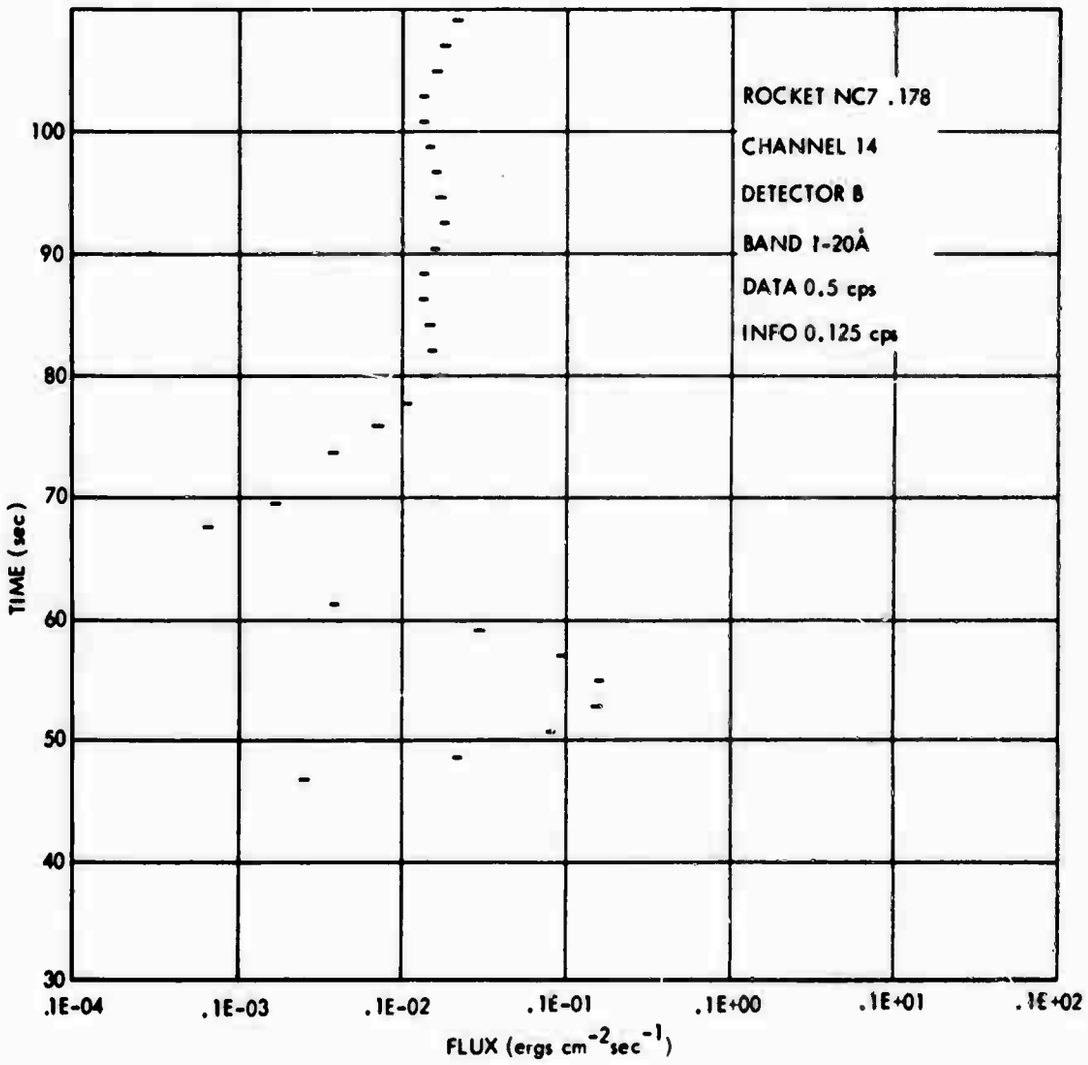

FIGURE 17. Flux Versus Time at Data Frequency 0.5 cps and Information Content 0.125 cps - 1-20Å Band, NC7.178 Detector B, Channel 14

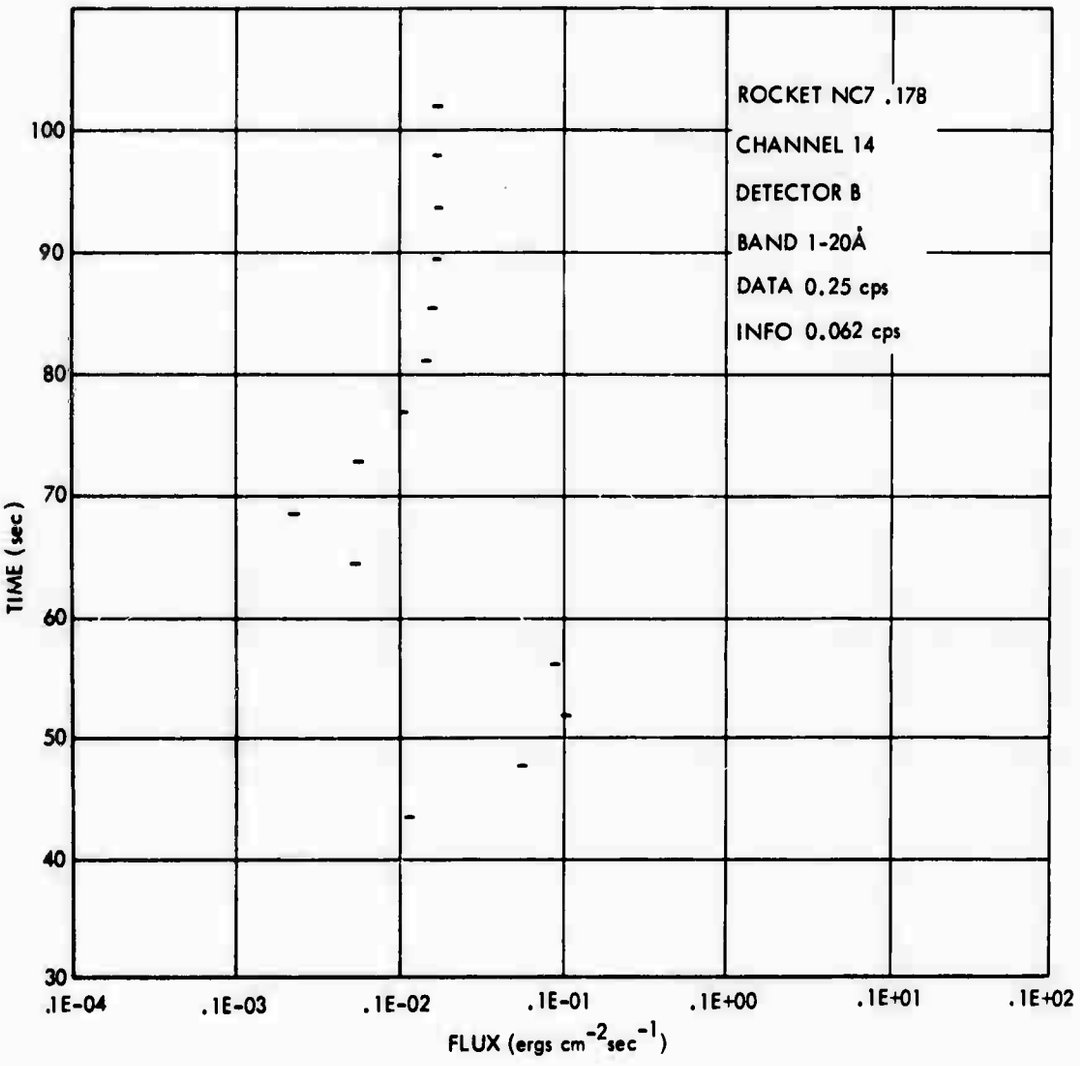

FIGURE 18. Flux Versus Time at Data Frequency 0.25 cps and Information Content 0.062 cps - 1-20Å Band, NC7.178 Detector B, Channel 14

D. FLUX VERSUS ALTITUDE

A next step in the determination is to convert flux, as a function of time of rocket flight, to flux as a function of altitude, using the altitude versus time characteristics given in Fig. 19.

The altitude history of flux measured by the three rocket experiments for the three wave bands of interest are shown in Fig. 1. These flux-altitude plots are derived from the data of flux versus time, smoothed to contain only information of frequency smaller than 0.125 cps.

Note that in interpreting density computations, in terms of flux and flux gradient, the vertical velocity of the rocket:

$$\frac{dz}{dt}(t) \lesssim 1.3 \text{ km sec}^{-1} \qquad (5)$$

corresponds to a speed of Mach 4; accordingly, flux altitude data are contained within a band of maximum wave number $k \simeq 0.1 \text{ km}^{-1}$. The atmospheric scale height implies atmospheric variations are expected within a band of maximum wave number $k \simeq 1/6 \text{ km}^{-1}$. Rocket nutation contains wave numbers as small as $k \geq 1/4 \text{ km}^{-1}$. All other undesirable wave numbers ($k > 1/4 \text{ km}^{-1}$) are those associated with rocket- and instrumentation-induced characteristics. These spectral differences provide a basis for distinguishing instrumentation artifacts from geophysical effects.

Some editing of flux versus altitude curves appears desirable before beginning density computations. In particular, all flux and flux values smaller than 10^{-10} are ignored. By accounting for all factors previously described, including computation results of variation coefficients described in the following paragraphs, credible ranges of measurement for each detector can be derived (Table 6). Data plotted in heavy lines in Figs. 1 to 3 inclusive, within the credible range limits described in Table 6, are deemed reliable for computing number density.

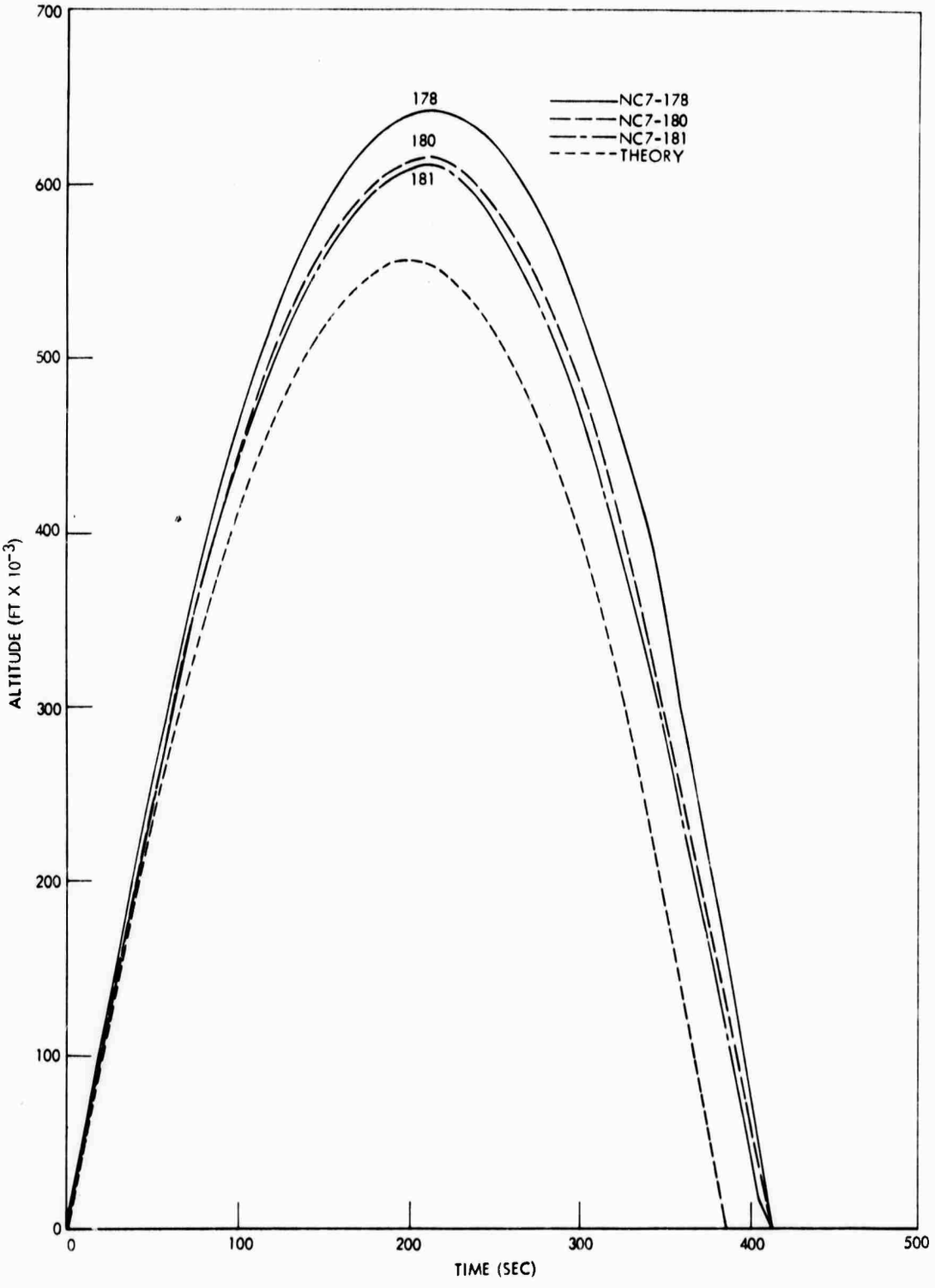

FIGURE 19. Altitude Versus Time

TABLE 6. CREDIBLE RANGES OF ALTITUDE AND TIME

Rocket	Channel	Detector	Plot Limit			
			Low Alt. Limit (Z)(km)	Upper Alt. Limit (Z)	Low Time Limit (t)	Upper Time Limit (t)(sec)
NC7.178	14	A	103	123	68.2	84.2
	14	B	107	123	71.3	84.5
	15	A	70	97	45.1	63.7
			97*	104*	63.7*	69.0*
		B	70	100	43.1	66.0
			100*	110*	66.0*	73.6*
	18	A	115	129	77.6	89.5
		B	122	141	83.4	100.7
NC7.180	14	A	98	121	66.7	85.8
		B	98	121	66.7	85.8
	15	A	70	93	46.5	62.9
			93*	105*	63.0*	72.3*
		B	70	95	46.5	64.4
			95*	105*	64.4*	72.3*
	18	A	108	140	74.7	104.4
		B	108	147	74.7	112.1
NC7.181	14	A	98	125	67.5	90.6
		B	98	125	67.5	90.6
	15	A	85	96	57.7	66.0
			96*	110*	66.0*	77.3*
		B	86	99	58.4	68.3
			99*	110*	68.3*	77.3*
	18	A	125	141	91.0	107.0
		B	117	144	83.1	110.4

*Reduced confidence - see Section III.A. & B.

E. ERROR ESTIMATES

An analysis of estimated error contributions (fractional uncertainties) to the measurement of flux by each detector of each channel is summarized in Table 7.

In the analysis, data variation coefficients for each detector used or for available representative samples of like kind are recorded, and they comprise several types including systematic variations in laboratory techniques for determining detector sensitivity and variations in:

- Sensitivities of individual detectors
- Gas gain in the time between laboratory calibration and time of flight
- Detector aperture area and shape of aperture function
- Gain in dc amplifiers
- Telemetry timing and other variations introduced by telemetry and digitizing processing.

Based on the premise that each of these contributions is independent of the others, the total variation coefficient of normalized ion current is computed from the rms of all contributions, for comparison with the measured variation coefficient of the current values determined from telemetered data. Results of the computed and measured variation coefficients of the normalized detector current are comparable in the case of each detector.

Variation coefficients of flux values over the credible range as determined by each single detector are also tabulated in Table 7. Differences between these variation coefficients and those of detector current reflect distortion introduced by smoothing and filtering processes in time.

The variation coefficient of measured flux data was determined in the following way.

The coefficient of variation, or fractional variation (i.e., the ratio of standard deviation to the mean) in the filtered flux

TABLE 7. ESTIMATED FRACTIONAL UNCERTAINTIES OF FLUX

		CONTRIBUTIONS TO ION CURRENT UNCERTAINTY (Coefficient of Variation)								NORMALIZED ION CURRENT UNCERTAINTY		FLUX UNCERTAINTY (Coefficient of Variation)	
Rocket	Channel & Detector	Measurement Technique (Meas)	Individual Efficiency (Meas)	Gas Gain (Meas)	Apert Area (Meas)	Ampl Gain (Meas)	Apert Funct (Meas)	Timing (Meas)	Telemetry & Digitizing (Meas)	Current (Comp)	Current (Meas)	Flux (Single Detector) (Meas)	Flux (Out of Atmos. Two Detectors) (Meas)
NC7.178	15A (Ly-α)	0.081	0.036	NA	0.12	0.02	0.028	0.16	0.017	0.23	0.20	0.10	0.07
	15B (Ly-α)	0.081	0.036	NA	0.12	0.02	0.061	0.16	0.017	0.22	0.22	0.04	
	18A (SR)	0.081	0.072	NA	0.05	0	0.058	0	0.024	0.13	0.12	0.20	0.026
	18B (SR)	0.081	0.072	NA	0.05	0	0.024	0	0.024	0.12	0.27	0.10	
	14A (1-20Å)	1.0	0.06	0.041	0	0.02	0.042	0	0.013	1.03	0.66	1.4	0.027
	14B (1-20Å)	1.0	0.06	0.041	0	0.02	0.050	0	0.013	1.03	0.77	1.1	
NC7.180	15A (Ly-α)	0.081	0.036	NA	0.11	0	0.034	0.20	0.004	0.24	0.38	0.03	0.19
	15B (Ly-α)	0.081	0.036	NA	0.11	0	0.019	0.20	0.004	0.24	0.46	0.03	
	18A (SR)	0.081	0.072	NA	0.05	0.02	0.054	0	0.004	0.13	0.11	0.20	0.25
	18B (SR)	0.081	0.072	NA	0.05	0.02	0.026	0	0.004	0.12	0.070	0.20	
	14A (1-20Å)	1.0	0.06	0.041	0	0.07	0.051	0	0.005	1.0	0.09	0.20	0.007
	14B (1-20Å)	1.0	0.06	0.041	0	0.07	0.082	0	0.005	1.0	0.14	0.30	
NC7.181	15A (Ly-α)	0.081	0.036	NA	0.16	0	0.028	0.22	0.006	0.29	0.047	0.01	0.07
	15B (Ly-α)	0.081	0.036	NA	0.16	0	0.06	0.22	0.006	0.29	0.010	0.01	
	18A (SR)	0.081	0.072	NA	0.05	0.07	0.058	0	0.005	0.17	0.29	0.10	0.054
	18B (SR)	0.081	0.072	NA	0.05	0.07	0.024	0	0.005	0.17	0.20	0.20	
	14A (1-20Å)	1.0	0.06	0.041	0	0.02	0.042	0	0.007	1.00	0.079	0.10	0.10
	14B (1-20Å)	1.0	0.06	0.041	0	0.02	0.050	0	0.007	1.0	0.038	0.20	

data is estimated as a function of time for rocket experiments NC7.178 in Fig. 20, NC7.180 in Fig. 21, and NC7.181 in Fig. 22. The error, as shown, is computed for 8-sec intervals within an altitude range near the credible ranges of altitude shown in Table 6.

Computation of fractional variation is based on a calculation, for each time increment T_t, of the difference between unfiltered flux values (XUF_t) and filtered flux values after hamming and decimations (XF_t), wherein t takes values from 1 to NP where NP is the number of points in the rocket data; N is determined for each T_t so that:

$$T_t + N \leq T_t + 8 \leq T_t + N + 1 \tag{6}$$

and the error is calculated as:

$$ER_t = \frac{\sqrt{\sum_{j=t}^{t+N} (XUF_j - XF_j)^2/(N+1)}}{\sum_{j=t}^{t+N} XF_j/(N+1)} \tag{7}$$

In addition to the fractional variation computed by the relation (7), a single coefficient of variation is calculated for the entire credible range.

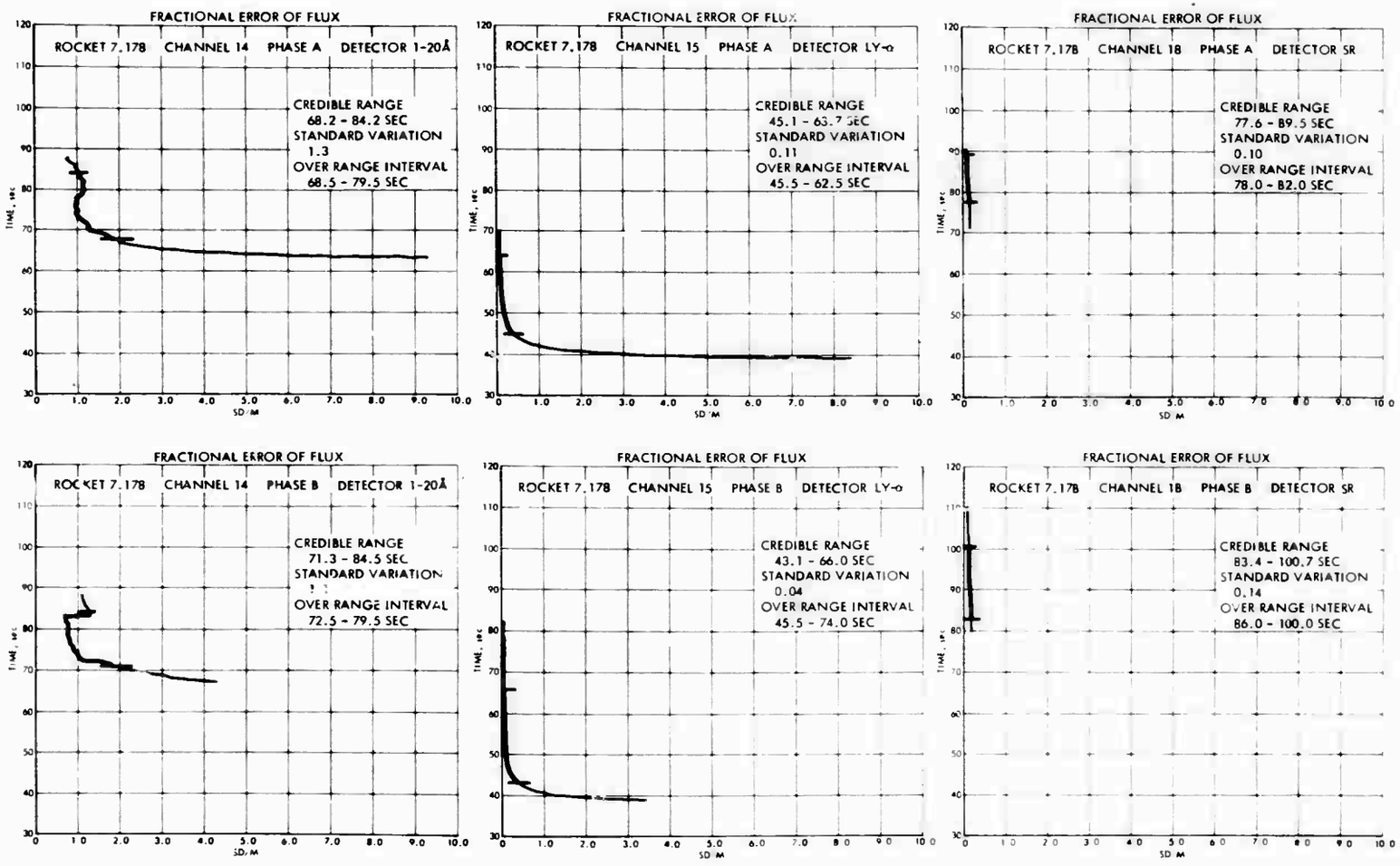

FIGURE 20. NC7.178 Flux Error Versus Time

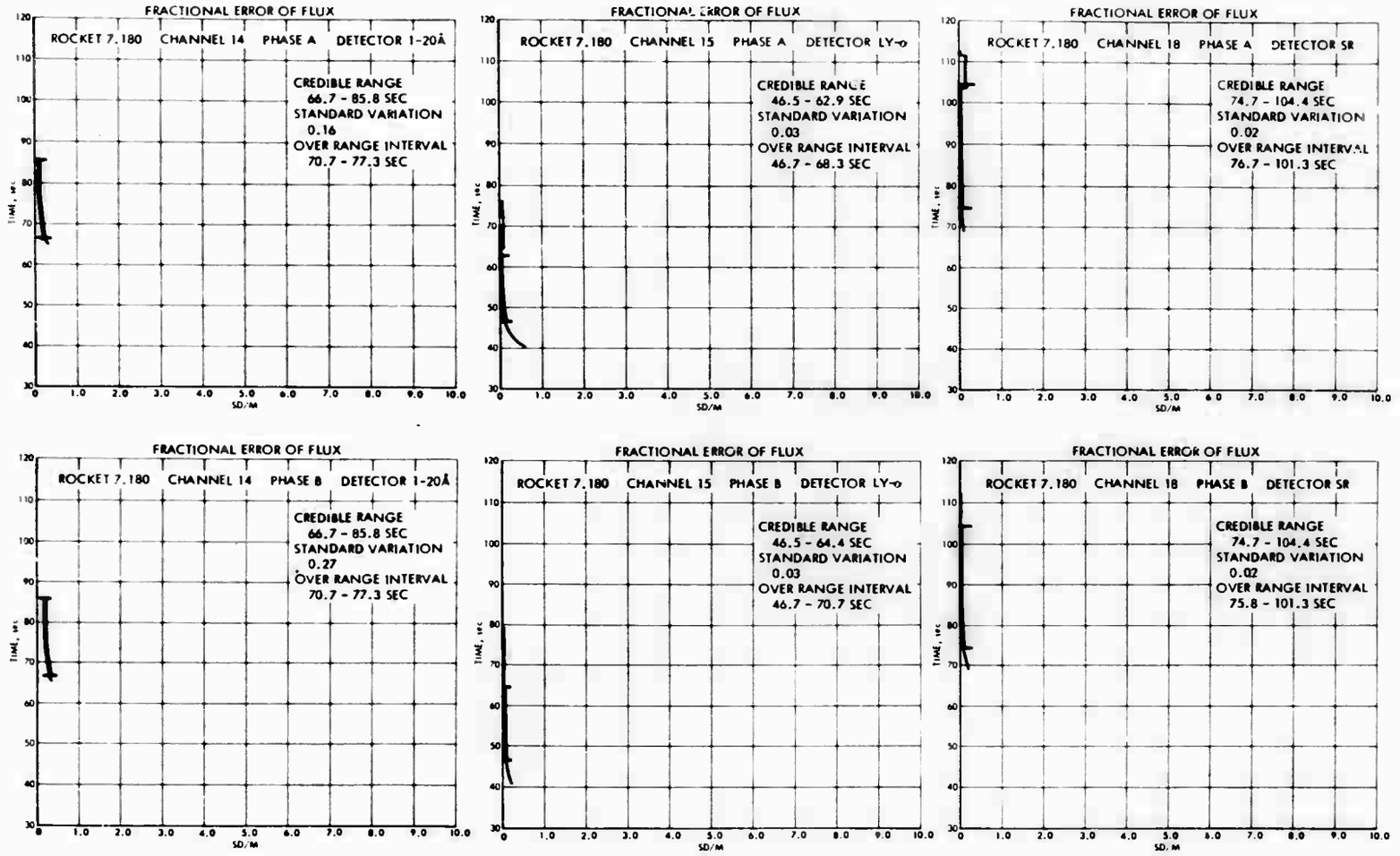

FIGURE 21. NC7.180 Flux Error vs. Time

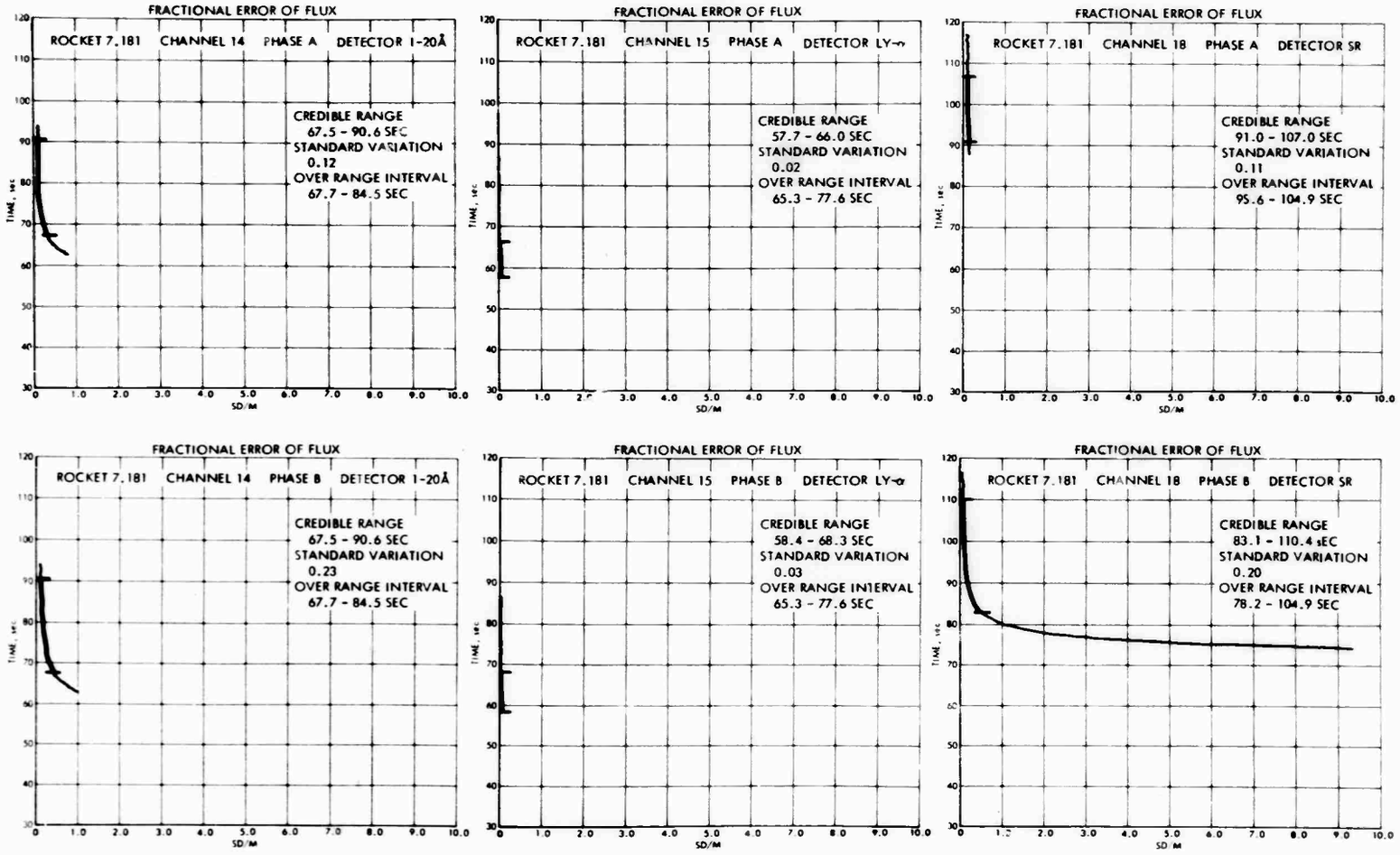

FIGURE 22. NC7.181 Flux Error vs. Time

BLANK PAGE

III. "TOTAL" PARTICLE AND O_2 DENSITY DISTRIBUTION

A. ANALYSIS OF DATA

Reduction of the solar flux absorption data is described in detail by Grobecker (1967b, 1967c, and 1967e). Briefly, the telemetry data of ion chamber signals continuously recorded at the ground station during the rocket flight were reduced in the following steps:

1. Digitized at 400 samples per second in terms of voltage of the rocketborne dc amplifiers
2. Converted by amplifier calibrations to ion chamber detector output current
3. Normalized to equivalent flux energy in the wavelength band of detector sensitivities, accounting for laboratory calibrations of detector current resulting from normally incident flux, variation of detector sensitivity when the flux is not normally incident, and the time history of individual detector changes.

Determination of equivalent flux energy also required the calculation of the effect of solar radiation, progressively hardening (mean wavelength within the band of detector sensitivity becomes shorter) as it penetrates deeper into the atmosphere, on the apparent spectral efficiency determined by laboratory calibration for each individual detector.

From data on flux E(z) as a function of altitude (Section II.D.), density of the "total" particle and O_2 content of the atmosphere may be computed. In this case, "total" particle content is taken to be:

$$n(tot) = n(N_2) + n(O_2) + \tfrac{1}{2}\, n(O) \ , \qquad (8)$$

since the X-radiation does not distinguish between the atomic and molecular form of oxygen. Density is computed by relation:

$$n(z) = \frac{dE/dz}{\bar{\sigma}(z)\, F(z)\, E(z)} \tag{9}$$

where $\bar{\sigma}(z)$ is the mean absorption cross section as a function of altitude, F(z) is the optical depth factor, and E is the solar flux intensity.

The evaluation of dE/dz(z) from the digitized values of flux E(z) again required careful band-limited filtering accomplished in the wave number domain by means of fast Fourier transforms (Cooley & Tukey, 1965). The band of wave numbers retained in the computation of dE/dz(z) included only those between 0 and 1/7 cycles per kilometer. In computing density in terms of flux and flux gradient, advantage is taken of the fact that major atmospheric characteristics are expected to be observed within an atmospheric scale height of 7 km to 10 km and, hence, are contained within a band of wave numbers less than k = 1/7 cp km. Rocket nutation is characterized by wave numbers larger than $k \geq 1/4$ cp km. All other undesirable wave numbers, $k > 1/4$ cp km, are taken to be those associated with rocket- and instrumentation-induced characteristics, and not geophysical ones. Data filtering in terms of these spectral differences provides a basis for distinguishing instrumentation artifacts from major geophysical effects, but it obscures observation of the fine structure of the atmosphere.

An essential in computing density distribution by Eq. 9 is the appropriate evaluation of the optical depth factor F(z). This factor approximates the secant of the solar zenith angle at small values of the angle, but also accounts for the apparent thickness of

the spherically shelled atmosphere at large zenith angles. Optical depth factors were calculated from tables and with methods described by Swider (1964), accounting for local solar zenith angles at times of the rocket flight, and an assumed model of atmospheric scale height H(z).

The mean absorption cross section, except for that of the H Ly-α line which is taken at a constant value of 1×10^{-20} cm^2 over the width of the line (Watanabe, 1958), is calculated by the relation:

$$\bar{\sigma}(z_i) = \frac{k \int_{1\text{Å}}^{8\text{Å}} P(\lambda,T_8)\,\sigma(\lambda) e^{-\sigma(\lambda)\int_{z_{i+1}}^{\infty} F(z)\,n(z)\,dz}\,d\lambda + \int_{8\text{Å}}^{30\text{Å}} P(\lambda,T_{30})\,\sigma(\lambda) e^{-\sigma(\lambda)\int_{z_{i+1}}^{\infty} F(z)\,n(z)\,dz}\,d\lambda}{k \int_{1\text{Å}}^{8\text{Å}} P(\lambda,T_8) e^{-\sigma(\lambda)\int_{z_{i+1}}^{\infty} F(z)\,n(z)\,dz}\,d\lambda + \int_{8\text{Å}}^{30\text{Å}} P(\lambda,T_{30})\,\sigma(\lambda) e^{-\sigma(\lambda)\int_{z_{i+1}}^{\infty} F(z)\,n(z)\,dz}\,d\lambda} \qquad (10)$$

where k = E(1-8Å)/E(8-30Å), the ratio of out-of-the-atmosphere fluxes of the 1-8Å and 8-30Å wave bands, as determined for the same hour by Explorer 30 satellite.

= 0.05 for NC7.181 and 0.0035 for NC7.178 & NC7.180.

$P(\lambda,T_8) = \lambda^{-5} [\exp(c/T_8\lambda)-1]^{-1}$

$P(\lambda,T_{30}) = \lambda^{-5} [\exp(c/T_{30}\lambda)-1]^{-1}$

$T_8 = 2(10)^6\ ^oK$

$T_{30} = 4(10)^6\ ^oK$

$c = 1.43879\ ^oK$

T = solar temperature

$\sigma(\lambda)$ = wavelength-dependent absorption cross section.

and $\int_{z_{i+1}}^{\infty} n(z)\, dz$ is derived from values of density in previous (higher altitude) computational steps. Relation 10 expresses recognition that the mean wavelength within the band of detector sensitivity becomes shorter as the solar radiation penetrates deeper into the atmosphere (hardening).

For 1-20Å determinations, solar temperature T is specified for two separate sources: 1-8Å at $T_8 = 8 \times 10^6$ and 8-30Å at $T_{30} = 2 \times 10^6$ ^oK.

For the 1-20Å radiation, the effective absorption cross section is due to the effect of both O_2 and N_2 molecules and to the effect of O atoms. The cross section of O atoms is half that of O_2 molecules. Therefore,

$$\sigma(\lambda) = 0.22\, \sigma_{O_2}(\lambda) + 0.78\, \sigma_{N_2}(\lambda) \qquad (11)$$

The wavelength-dependent cross section $\sigma(\lambda)$, used in determining mean cross section $\bar{\sigma}(z)$ by means of Eq. 10, is given in Table 8 utilizing data of Hinteregger et al. (1964).

For the SR continuum, values of wavelength-dependent absorption cross section $\sigma(\lambda)$ given in Table 9 (Hinteregger et al., 1964) are used to compute the mean absorption cross section $\bar{\sigma}(\lambda)$ over the band of detector sensitivity for radiation in the band of a solar source at temperature 4800 ^oK. This computation uses an equation analogous to Eq. 10 with a single term on the right-hand side numerator and denominator.

TABLE 8. ABSORPTION CROSS SECTION $\sigma(\lambda)$ IN 1-20Å RANGE

λ(Å)	$\sigma_{O_2}(cm^2)$	$\sigma_{N_2}(cm^2)$	$\sigma(\lambda)$
1 - 3	0.002×10^{-18}	0.0015×10^{-18}	0.0015×10^{-18}
3 - 5	0.012×10^{-18}	0.0065×10^{-18}	0.0075×10^{-18}
5 - 10	0.075×10^{-18}	0.045×10^{-18}	0.040×10^{-18}
10 - 15	0.27×10^{-18}	0.15×10^{-18}	0.171×10^{-18}
15 - 22	0.7×10^{-18}	0.36×10^{-18}	0.42×10^{-18}
22 - 31	0.09×10^{-18}	1.0×10^{-18}	0.80×10^{-18}

TABLE 9. ABSORPTION CROSS SECTION $\sigma(\lambda)$ IN SR CONTINUUM

λ (Å)	$\sigma(\lambda)$ (cm^2)
1325 - 1375	5.8×10^{-15}
1375 - 1475	14.3×10^{-18}
1475 - 1525	11.3×10^{-18}

As in the case of flux values depicted in Figs. 1, 2, and 3 (Section II), density determinations have altitude ranges of best and reduced credibility. Diminishment, from the best credibility shown by heavy lines in Figs. 1, 2, and 3, is based on one of several considerations:

1. Slope of the flux value's logarithm versus integrated number density (absorbing particles, per cm^2, of

gas between sun and detector) changes rapidly, indicating an unexplainable change of mean absorption coefficient.

2. Flux values are physically inconsistent.

3. Density determinations from the several flux bands are mutually inconsistent.

Altitude ranges for which measurements of density are credible (Table 6, Section II.D.) are based on these considerations. Those which reflect reduced confidence are marked with an asterisk in Table 6.

B. DENSITY VERSUS ALTITUDE

1. Absorption Measurements

Values of density computed, with Eq. 9, as a function of altitude are shown for NC7.178, NC7.180, and NC7.181 in Figs. 23, 24, and 25, respectively. Data points for each of two detectors (A and B), for each wave band measured by the three experiments, are indicated separately by symbols. Also shown in the figures, by horizontal bars, are the limits of the range of credible data. These limits are within the wider range of data that were analyzed computationally but included analyzed points in adjacent ranges believed, for reasons given in this report, not representative of the geophysical domain. Representations of density, taken as a mean of the two detector measurements in each band, are indicated by thin lines in the figures.

Examples of the application of the criteria for credible ranges listed in Table 6 (Section II) are found in the flux values and semilog plots of flux versus integrated number density in Figs. 1, 2, and 3 and the density values of Figs. 23, 24, and 25. As mentioned earlier (Section II.A.), change of slope in the semilog plot of flux measured by Channel 15 at particular altitudes was noted in records; also, in determining density from H Ly-α flux values, an apparent

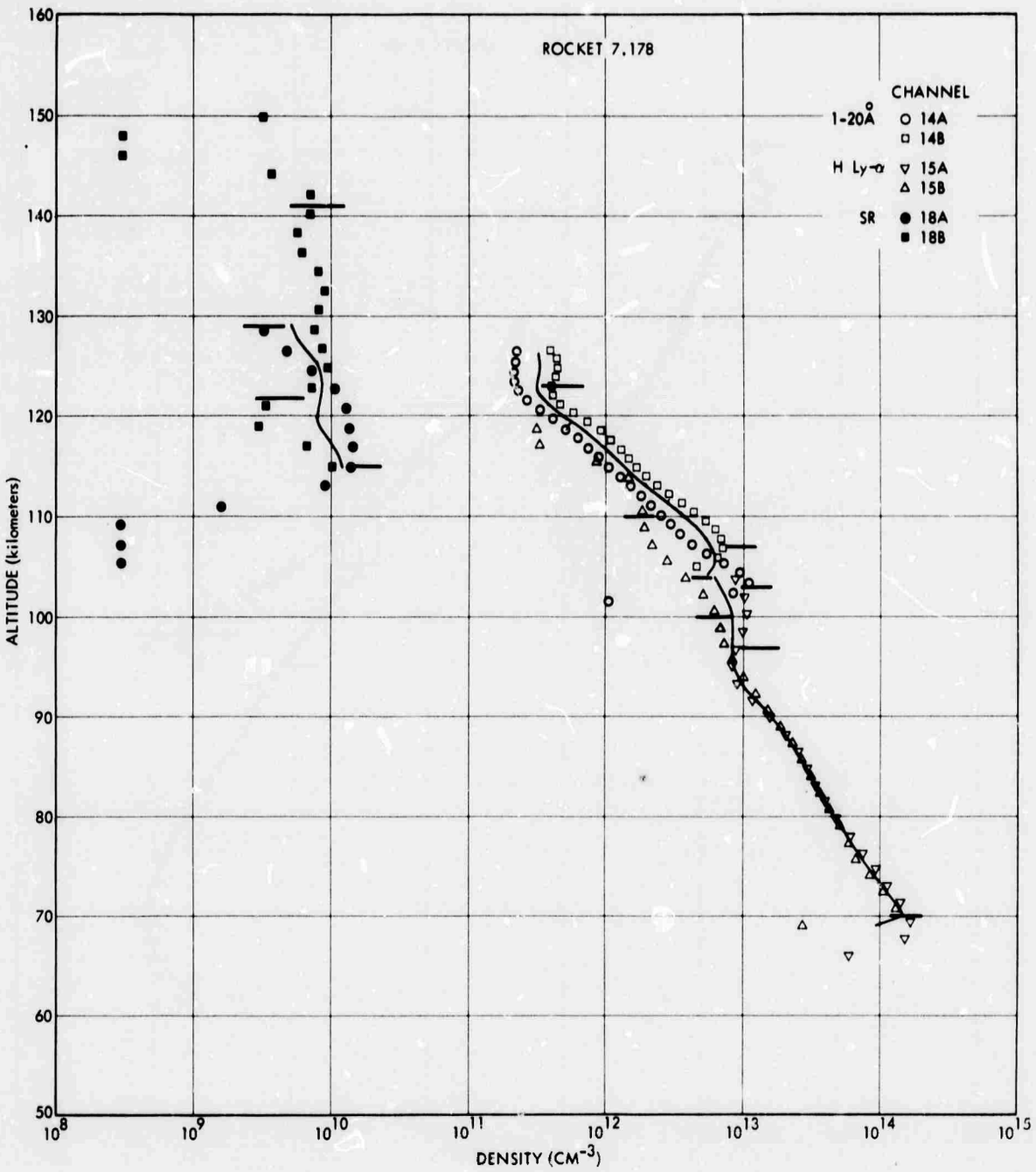

FIGURE 23. Density versus Altitude - NC7.178

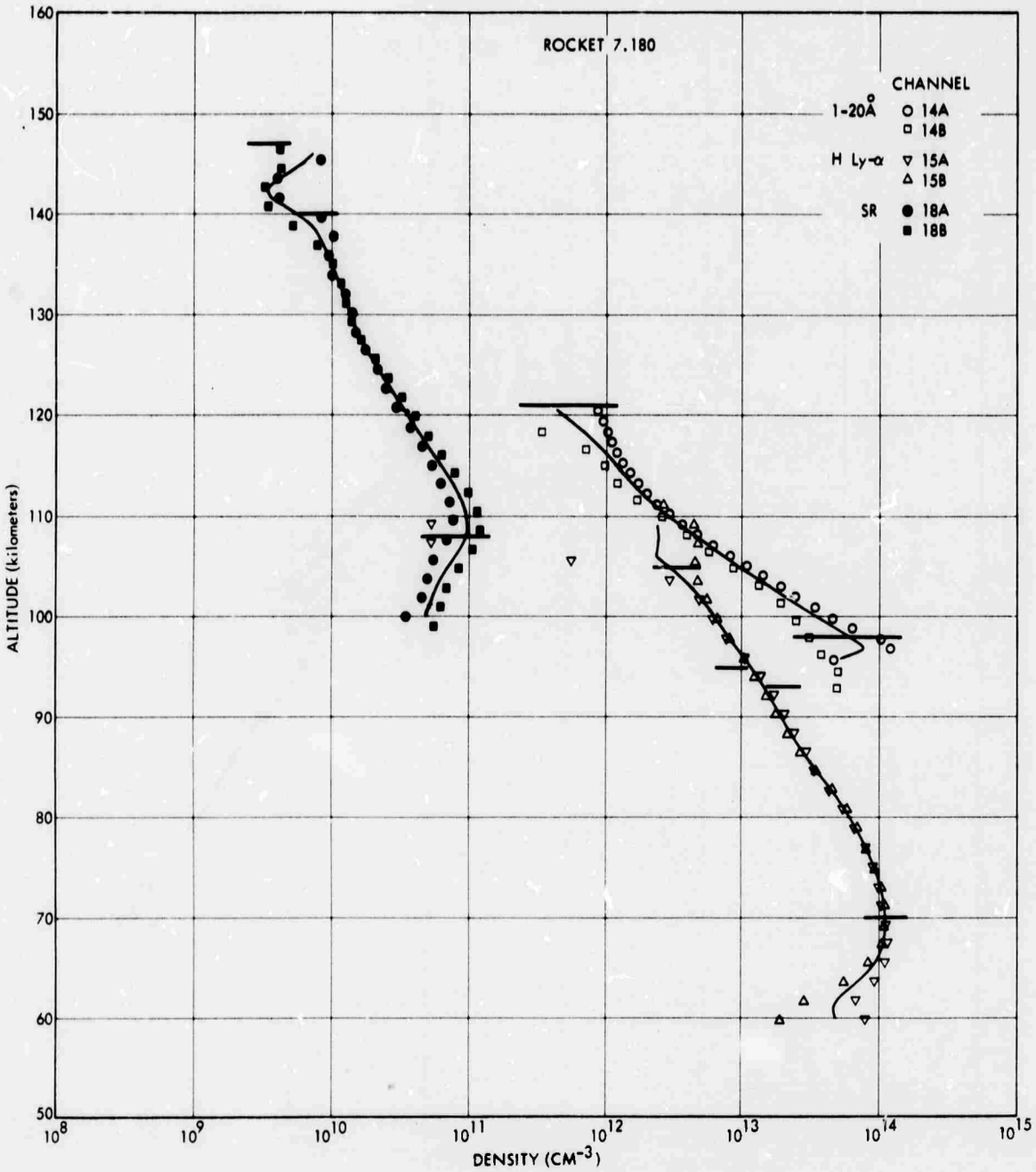

FIGURE 24. Density versus Altitude - NC7.180

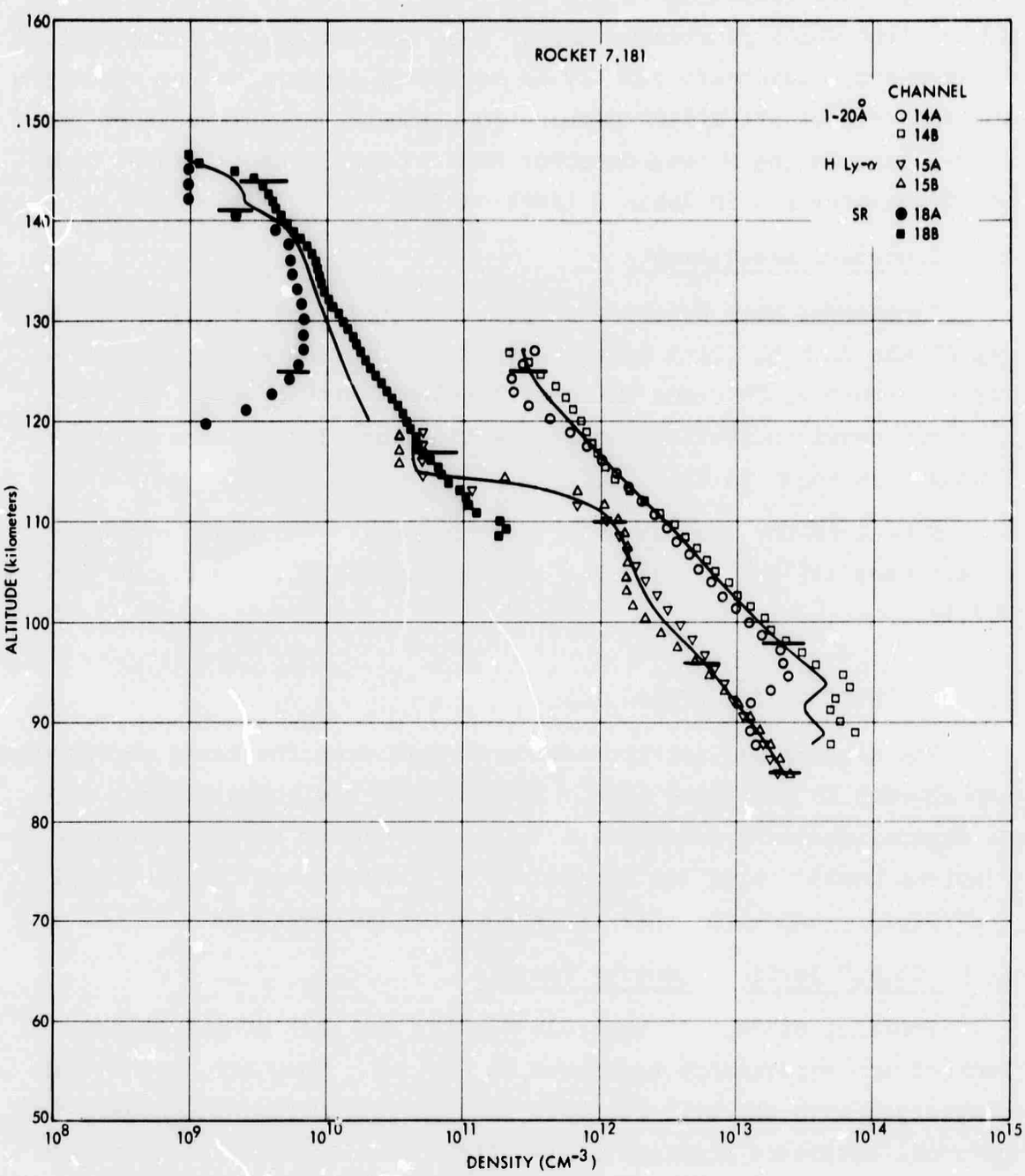

FIGURE 25. Density versus Altitude - NC7.181

bulge of O_2 density occurred at high altitudes. As stated in Section II.A., this bulge is thought to be the effect of absorption contamination by other radiation (e.g., solar Si III line at 1206.5Å) in the H Ly-α line which penetrates deeply into the atmosphere. The 1206.5Å solar energy disappears quickly as radiation penetrates the absorbing atmosphere, but its effect perhaps contaminates measurements of the H Ly-α line by the H Ly-α detector down to the lower altitudes indicated by asterisks in Table 6 (Section II).

2. Ionosonde Measurements

Ionosondes were operated at Fort Churchill and at Eglin on the day of the launch. Data were analyzed by the ESSA Research Laboratories, Boulder, Colorado (Wright, 1966). A plot of the ionosonde electron-density distribution at the time and place of the three launches is shown in Fig. 26.

Note that the gradient of electron density increases greatly at altitude 118 km for NC7.178, 107 km for NC7.180, and 108 km for NC7.181.

C. GEOPHYSICAL INTERPRETATION

The geophysical interpretation of data from the three rocketborne experiments is described here. Present data are compared with data on neutral particle densities determined by other experimenters, with electron density profiles determined by ionosonde in the same altitude region, and with other representative observations.

1. "Total" Particle Density Profile

Profiles of "total" particle density for each of the three rocketborne experiments are shown in Fig. 27. They are depicted in comparison with the U.S. Standard Atmosphere (1962) and COSPAR International Reference Atmosphere CIRA (1965), using models appropriate to conditions for the launch day (10.6 cm radiation flux of about 85×10^{-22} w m^{-2} Hz^{-1} and geomagnetic index $A_p \sim 4$). Also included in Fig. 27, for comparison purposes, are data reported from mass

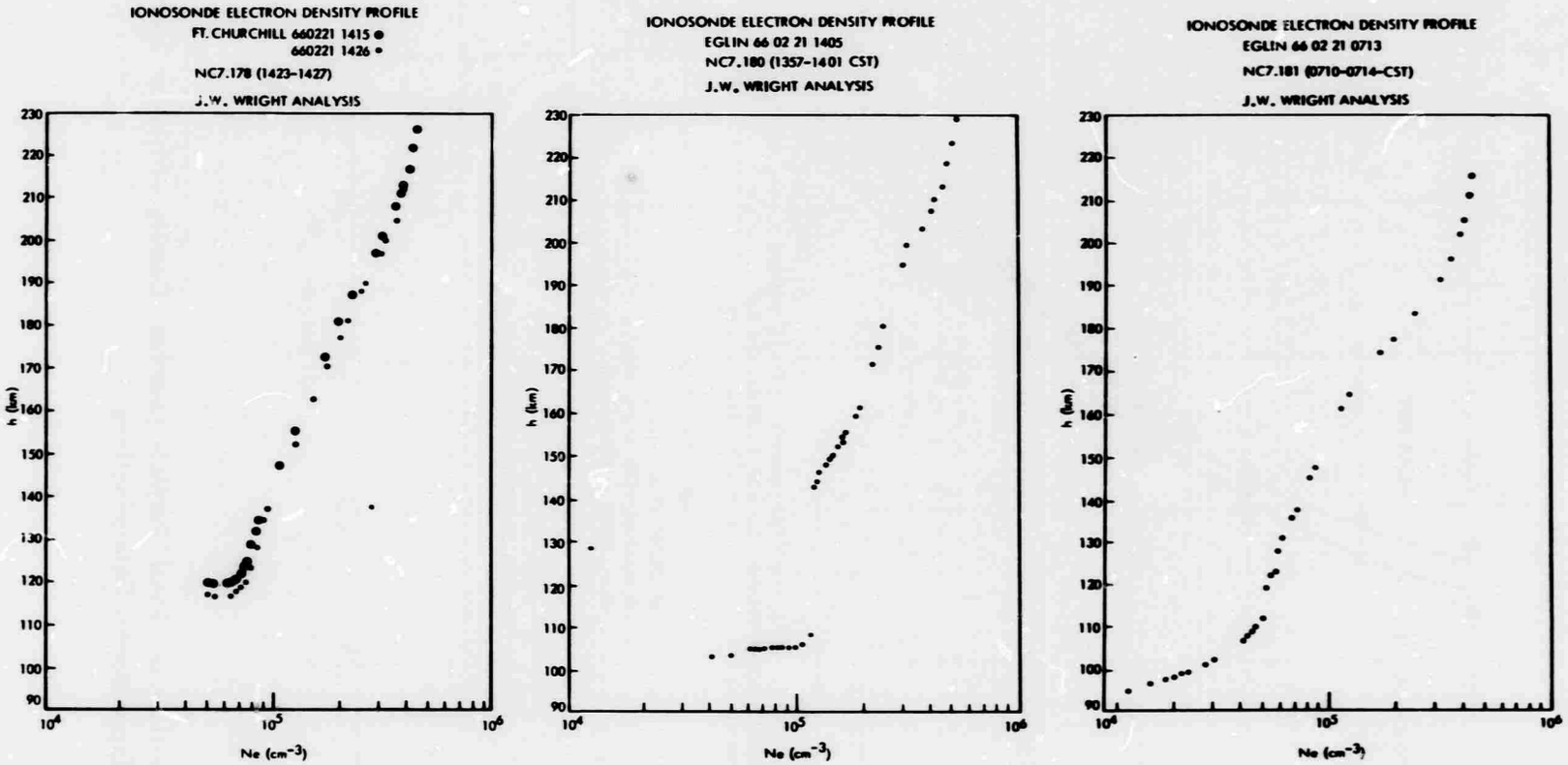

FIGURE 26 Ionosonde Electron Density Profiles--Fort Churchill and Eglin

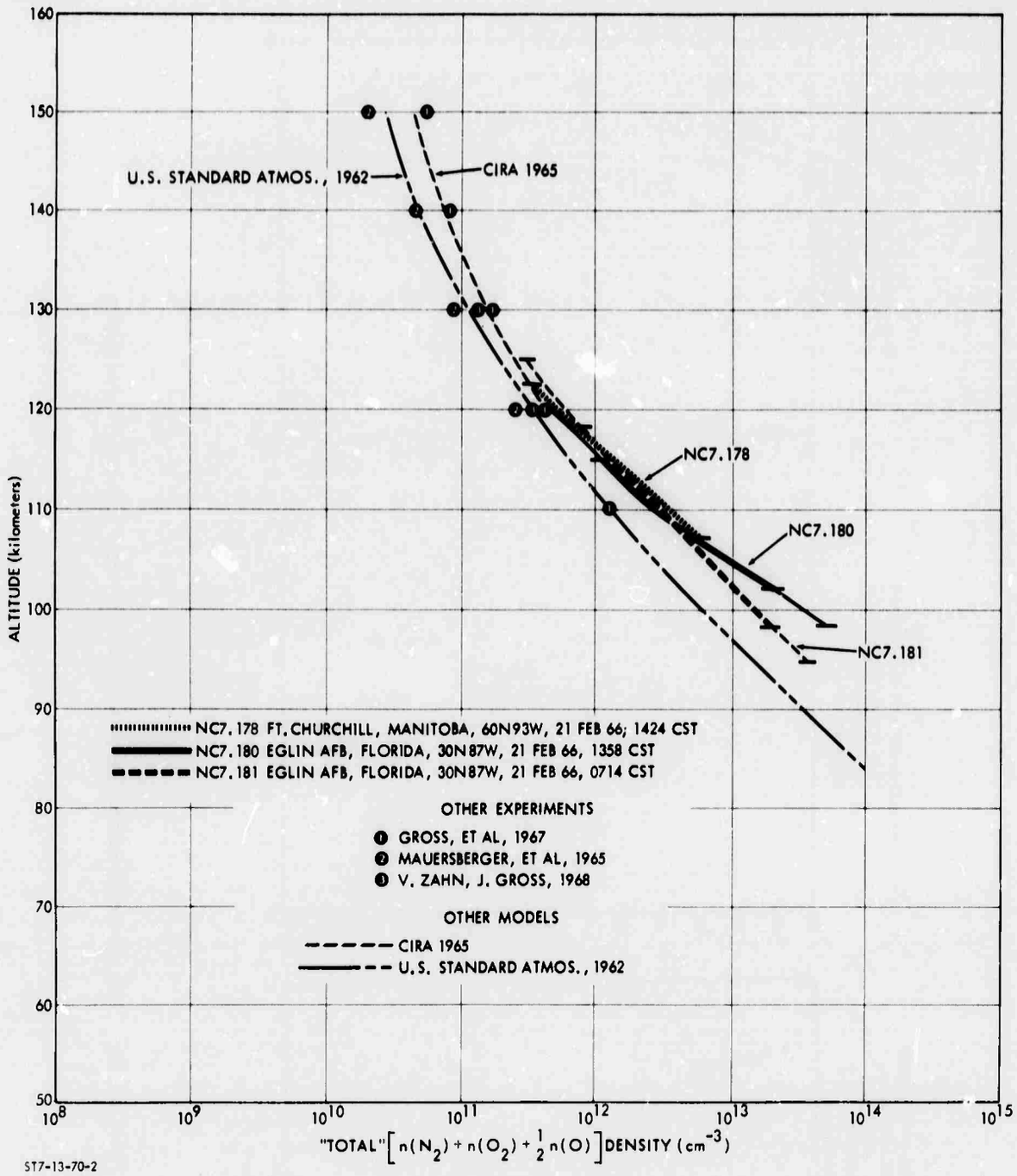

FIGURE 27. Comparison of "Total" Particle (number) Density with other Theoretical and Experimental Determinations

spectrometer measurements made at Fort Churchill on 12 December 1966 (Gross, Offermann and von Zahn, 1967), and in Sardinia on 11 December 1965 (Mauersberger, Muller, Offermann, & von Zahn, 1965), and data reported by von Zahn and Gross (1968). The "total" particle density [$n(N_2) + n(O_2) + \frac{1}{2} n(O)$] profiles are based on the assumption that the solar source of X rays in the 1-20Å band is at a temperature of 2×10^6 °K and the solar source of X rays in the 1-20Å band is at a temperature of 8×10^6 °K. Flux data for density computations were filtered to include only frequencies smaller than 0.125 cps. Data of greatest credibility are shown with a heavy line; those of lesser credibility with a thin line.

As evidenced in Fig. 27, determinations of "total" particle density for the three rocketborne experiments at about 120 km are consistent with each other and with the CIRA 1965 determination. Density values at lower altitudes are higher for the present experiments than those attributed by the U.S. Standard Atmosphere (1962). But they are consistent with the high temperature from 70 to 125 km, implied by the smaller slopes d ln n/dz displayed with mutual consistency by the profiles of both "total" and O_2 density below 100 km.

2. O_2 Particle Density Profiles

Profiles of O_2 particle density for each of the three rocketborne experiments are shown in Fig. 28. However, O_2 density determinations derived by two SR detectors of NC7.178 and by one SR detector of NC7.181 are omitted from Fig. 28. These determinations, shown in Figs. 23 and 25, appear dubious because of the small signal strength recorded by the detectors in question.

Heavy lines in Fig. 28 denote experimental data of best credibility; thin lines denote data of diminished credibility. Horizontal bars demark the credibility ranges.

Since the absorption of H Ly-α radiation may be contaminated by absorption of the Si III line at 1206.5Å, the densities are suspect when determined from H Ly-α absorption above the 104, 105, and 110 km altitudes (and possible above 97, 93, and 96 km) for NC7.178, NC7.180,

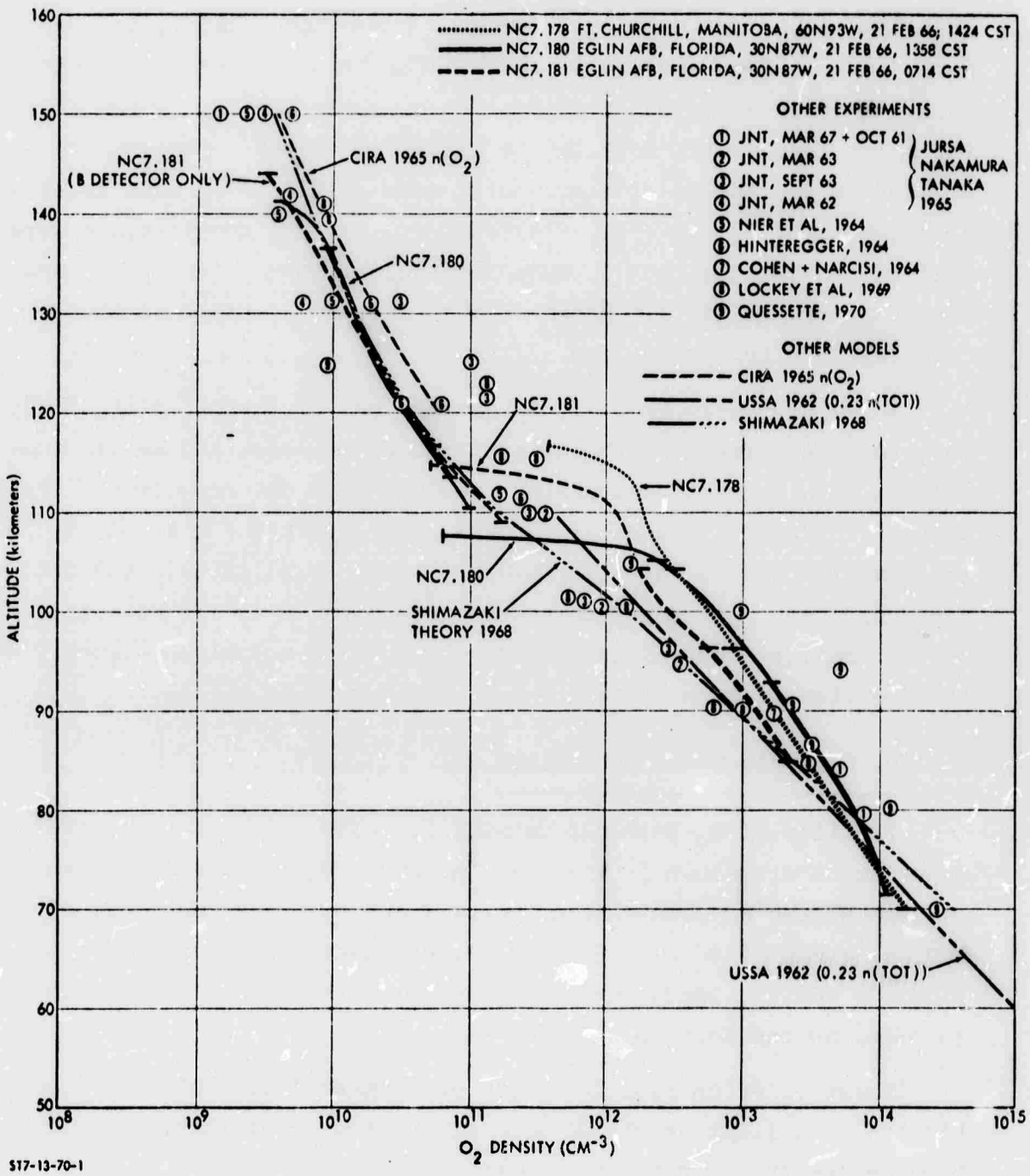

FIGURE 28. Comparison of O_2 Number Density with Other Theoretical and Experimental Determinations

and NC7.181, respectively. This contamination by the Si III line (2 percent of the out-of-the-atmosphere energy) may account for the bulge of density appearing in the H Ly-α derived profiles of NC7.178 and NC7.181.

Despite the questionability of the bulge and the limitation of the dynamic range of the duplicated detection systems, which prevented each detector type from covering the whole range of the O_2 density step, the H Ly-α detectors indicate a steep gradient of O_2 density between 108 and 117 km; this is well within the dynamic range of density determination and is reasonably consistent with the SR determination of density. In the case of NC7.181, the overlap between the minimum limit of density determinable by H Ly-α absorption and maximum limit of density determinable by SR absorption may be attributed to a lag introduced by the filtering process. Although the existence of the step in O_2 density is apparent from the data, its altitude is uncertain within perhaps 4 km.

Also shown in Fig. 28, for comparison purposes, are data points reported by other observers (Lockey et al., 1969 and Quessette, 1970), and standard atmosphere models [CIRA 1965 model appropriate to a 10.6-cm flux of about 85 w m^{-2} Hz^{-1}, U.S. Standard Atmosphere 1962, and the T. Shimazaki (1968) model which accounts for isomeric diffusion due to chemical, temperature, and neutral particle gradients].

The O_2 determination of the three NRL experiments agrees generally with that of other experimenters; the latter data, however, do not show the rapid change of O_2 density with change in altitude near 110 km. This surprising feature of the experimental results is not reflected in either the compilations of solar geophysical data by the U.S. Department of Commerce (1966) or COSPAR Standard Atmospheres (CIRA, 1965). It may be a temporary varying phenomenon.

Lockey, Horton and Rofe (1969) reported a band of almost constant density appearing over an interval of altitude. Quessette (1970) reported data that suggest a density step near 105 km. Relatively few measurements of the molecular oxygen distribution

have been made in the critical region of the atmosphere between 100 and 120 km. Consequently, it is possible that either a constant density over a range of altitude (as described by Lockey et al., 1969), or a very small-scale height (rapid change of an order of magnitude in short distance), as observed by these experiments, is possible in the terrestrial atmosphere. Since measurements made in this region, in general, have poor height definition, the profile over the critical range from 100 to 120 km is not clearly defined.

3. Electron Density Profiles

The electron density profiles shown in Fig. 26 indicate the following features: at 0710 CST (the time at which NC7.181 was launched at Eglin), the solar zenith angle was nearly the same as that at Fort Churchill at 1423 CST (the time at which NC7.178 was launched). However, the E-region above 120-km altitude is more intensely ionized at Fort Churchill, presumably because of the longer solar radiation exposure. Comparison with the Eglin data obtained at 1357 CST (time of NC7.180 launch) reveals that at similar midday local solar times, the lower altitude, smaller zenith-angle location (Eglin) is characterized by a greater degree of E-region ionization.

4. Temperature and Wind Profiles

Temperature (U.S. Standard Atmosphere 1962) and wind profiles (Kochanski, 1964, 1966) are shown in Fig. 29. Note that these were not measured at the same time as the absorption and ionosonde measurements, but represent the latitudes and season in which the NRL experiments took place.

Under meteorological conditions, the criterion for turbulence maintenance is commonly expressed in terms of the dimensionless Richardson's Number, Ri, which is the ratio of the restoring buoyancy force per unit length of vertical displacement, to the square of the wind shear.

Instability in the presence of a density or temperature gradient under gravity is implied by Richardson number:

$$Ri < Ri_{crit} \sim 0.04 - 1 \qquad (12)$$

where Ri_{crit} is a critical value of Richardson number (Schlichting, 1960).

Based on Richardson number data (Fig. 29), it is concluded that in the lower thermosphere, near the critical limit for suppression by the temperature gradient, turbulence may be likely, particularly in the 100- to 110-km altitude range. The cessation of mixing due to turbulence may determine the O_2 density step. Below the step, turbulent mixing facilitates the third-body recombination of atomic oxygen. Above the step, the slower mixing by diffusion implies slower recombination, an enhanced atomic oxygen population, and a reduced molecular oxygen population.

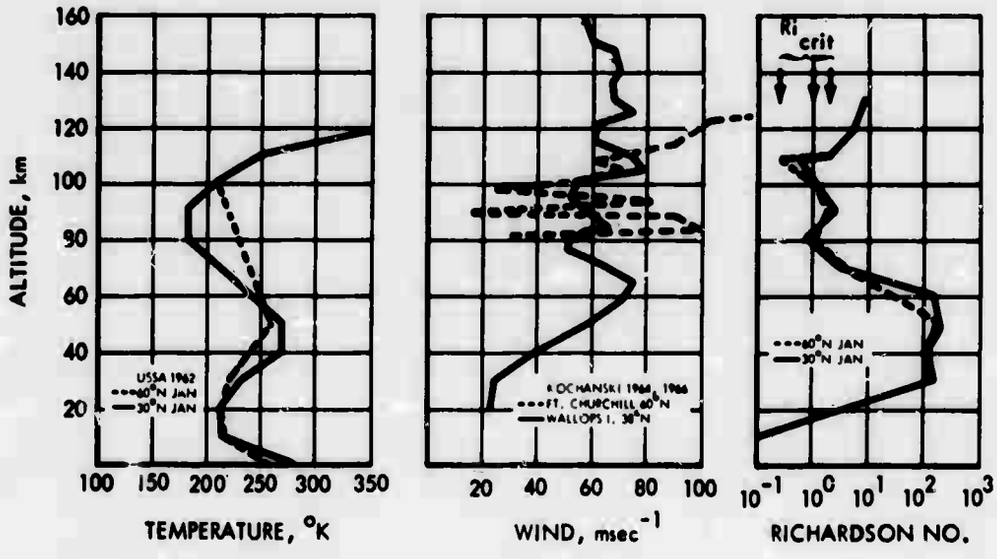

FIGURE 29. Temperature, Wind Speed, and Richardson Numbers as a Function of Height

5. Comparison of Homopause and Turbopause Altitudes

An altitude comparison of the step in O_2 density (called "homopause", signifying the altitude region below which the atmospheric composition is essentially constant) is given in Table 10. The homopause altitude is compared with that of the E-layer bottom (marked by the sharp increase of electron density observed by ionosonde), and with the upper altitude of thermosphere turbulence (called "turbopause") indicated by a Richardson number based on representative wind and temperature gradients. The results show agreement within the uncertainty of the measurement: the discrepancy between absorption and ionosonde evidence of the homopause-turbopause is about one km in the morning case of the Eglin location, and almost exact for the midday case at Eglin and the midday case at Fort Churchill.

6. Theory of $n(O_2)$ Step by Nonisomeric Diffusion

Tchen (1969) has given a theoretical explanation to account for the anomalous reduction of O_2 density near 110 km by turbulent diffusion processes. He finds that the density n(z) may vary as a function of altitude z as

$$n(z) = N(z)\, f(z) \,, \tag{13a}$$

where

$$N(z) = \frac{n_o T_o}{T(z)} \exp\left[-\int_{z_o}^{z} dz(Y+H^{-1})\right] \tag{13b}$$

and

$$f(z) = \exp\left[-\int_{z_o}^{z} dz\beta\left(\frac{1}{H} + \frac{d\ln T}{dz}\right)\right] ; \tag{13c}$$

TABLE 10. COMPARISON OF ALTITUDES OF HOMOPAUSE BY ABSORPTION AND IONOSONDE OBSERVATIONS AND OF TURBOPAUSE BY REPRESENTATIVE TEMPERATURES AND WINDS

ROCKET EXPERIMENT	LAUNCH LOCATION	VEHICLE PASSAGE THROUGH $z = 100$ km			ABSORPTION OBSERVATION OF HOMOPAUSE ALTITUDE	IONOSONDE OBSERVATION ALTITUDE OF E-LAYER BOTTOM	REPRESENTATIVE ALTITUDE OF TURBOPAUSE**
		Δt (sec)	GMT* hr min	SOLAR ZENITH ANGLE (deg)	$z_h(\pm\Delta z_h/2)$ km		
NC7.178	Ft. Churchill, Manitoba (58°N 93°W)	70	20 24.34	75	117 ± 2	118 ± 2	104.5 ± 3.5
NC7.180	Eglin, Fla. (30°N 87°W)	74	19 58.23	49	107 ± 2	107 ± 2	104.5 ± 3.5
NC7.181	Eglin, Fla. (30°N 87°W)	74	13 10.82	83	115 ± 2 $\bar{z}$ = 113 ± 7	108 ± 4	104.5 ± 3.5

*GMT = Greenwich Mean Time

**Based on USSA 1962, January temperatures and Kochanski (1964, 1966) winds, so that Richardson No. implies turbulence.

also, $n_o = n(z = z_o)$; $T_o = T(z = z_o)$

$$\beta = \frac{D_{nn} - D_{nT}}{D_{mol} + D_{nT}} \tag{14a}$$

In Eq. 13, the effect of chemical change is accounted for by

$$\underset{\sim}{Y} = \frac{\underset{\sim}{X}}{n(D_{mol} + D_{nT})} \tag{14b}$$

where X = chemical reaction wherein $\nabla \cdot X_a$ is rate of production of density.

Tchen finds two diffusion coefficients effective in addition to the molecular diffusion coefficient D_{mol}. These are D_{nn} and D_{nT}, based on an autocorrelation of two density fluctuations or on a cross-correlation between a density fluctuation and a temperature function giving an eddy temperature diffusion coefficient:

$$D_{nn} = \frac{KT}{m} \int_0^\infty dt \, \frac{\overline{n'(o)\, n'(t)}}{n^2} \tag{15a}$$

and an eddy mass diffusion coefficient:

$$D_{nT} = \frac{KT}{m} \int_0^\infty dt \, \frac{\overline{n'(o)\, T'(z)}}{nT} \tag{15b}$$

Also, the scale height is given by

$$H = \frac{KT}{mg}$$

If the diffusion is "isomeric," i.e.,

$$D_{nT} = D_{nn} \text{ or } \beta = 0 \qquad (16)$$

the solution (13a) degenerates to (13b) with the reduction factor $f(z) = 1$. The solution (13b) is, in such a case, a smooth function decreasing with altitude in the manner exhibited by the U.S. Standard Atmosphere (1962).

In most cases of turbulent atmosphere, the diffusion is not isomeric, and $D_{nT} < D_{nn}$, so that $\beta > 0$.

Under such a circumstance of "nonisomeric" diffusion, the difference $D_{nn} - D_{nT}$ plays a role in the distribution of n. One expects this effect to occur in a region where the turbulent motion is the strongest.

Since the reduction factor f(z) does not contain the chemical effects, it can be calculated independently. A reduction factor of 10 in an interval of the scale height requires that $\beta = 1.7$, or that

$$D_{nT} = 0.35\ D_{nn}\ , \qquad (17)$$

a situation which is not impossible in the turbulent atmosphere. The theory is elaborated by Tchen (1970).

The anomalous reduction of O_2 near 110 km observed in the measured data reported in Fig. 28 may correspond to the effect of the nonisomeric diffusion ($D_{nn} > D_{nT}$) by turbulent movements.

7. Credibility of Geophysical Determinations

The credibility of the geophysical observations described in the previous paragraphs is weakened by three considerations:

a. The step in $n(O_2)$ at 110 km is not reported by other experimenters and is not traced reliably over its whole range by a single instrument in the NRL rocket experiments reported here.

b. Density values n(tot) in the range 100 to 120 km appear larger than given by extrapolation downward of mass spectrometer measurements above 120 km.

c. Temperatures between 70 and 100 km appear to be larger than given by the standard atmosphere models.

Considerations reinforcing the credibility are:

a. There is redundancy of measurements. Each wave band channel in each rocket vehicle employed two detectors and yielded similar results. Three rocket experiments each yielded analogous results, making allowance for expected geophysical variations due to differences of time and site.

b. The O_2 density data fits those measured by other experimenters. At altitudes less than 110 km, $n(O_2)$ is approximately 22 percent of the "total" particle density, as may be expected in a homogeneous atmosphere.

c. The base of the E-layer, as measured by simultaneous ionosonde at the same time as the absorption measurements, corresponds in altitude with the O_2 density step (in two cases, closely; in one case, approximately).

d. Representative wind and temperature profiles indicate a narrow zone of turbulence may be expected just below the

O_2 density step. This local zone of turbulence, with effects described analytically by Tchen (1970), provides a mechanism for the mixing to a homogeneous atmosphere below the turbopause-homopause. Above the turbulence zone, where diffusion is the sole mixing mechanism, the atmosphere becomes inhomogeneous; here, atomic oxygen, produced by dissociation of O_2 but with recombination (principally by a three-body reaction) reduced, becomes a significant constituent of the atmosphere. Below the turbulence zone, enhanced mixing depopulates atomic oxygen by the more effective three-body recombination.

e. Atmospheric temperatures are similar as determined at the same altitudes by different detectors. This is evidenced in the slopes of density profiles for both O_2 and "total" particles, since the temperature of the atmosphere is, except at the O_2 density step, inversely proportional to the logarithmic density gradient.

f. Flux data of measurements outside the effectively absorbing atmosphere fit other observations.

8. Summary

Important geophysical features of the experiments are summarized as follows:

a. A step of O_2 density, $n(O_2)(z)$ exists at altitude 113 ± 7 km on 21 February 1966. There is no comparable slope discontinuity of "total" particle density, n(tot). The step is believed to mark the homopause.

b. The homopause is higher at times of smaller solarization. Two experiments at like latitudes, but different times of day, show the homopause to be

higher when the sun is farther from the zenith. Two experiments at like times, but at different latitudes, show the homopause to be higher at the higher latitude. Two experiments with comparable solar zenith angles show the homopause altitudes to be similar.

c. Homopause generalizations derived by absorption measurements are corroborated by ionosonde-derived electron density profiles, showing the marked slope change identified as the base of the E-layer. The E-layer base seems to correspond with the homopause determined by the step in O_2 density, $n(O_2)(z)$.

d. Wind and temperature profiles, representative of the location and season of, but not simultaneously measured with, the absorption and ionosonde experiments, indicate that a zone of strong wind shear tending to turbulence may exist (on 21 February 1966) just below the observed homopause at from 101 to 108 km. The upper bound of such a shear-induced turbulence perhaps marks the turbopause.

e. The "total" particle density $\{[n(N_2)] + N(O_2) + \frac{1}{2} n(O)]\}$ in the 100- to 125-km altitude region exceeds that determined by mass spectrometer measurements, and represented by the U.S. Standard Atmosphere (1962), by a factor of about two.

f. Atmospheric temperatures, roughly determined to be in the 150 to 375 °K range for 70- to 150-km altitudes, are lar er at altitudes below 120 km than those of the U.S. Standard Atmosphere (1962) and CIRA (1965).

REFERENCES

AFCRL Geophysics and Space Data Bulletin, Vol. III, No. 1, A. Carrigan and N. Oliver, eds., 1966.

Blackman, R. B. and J. W. Tukey, The Measurement of Power Spectra, Dover Publications, Inc., New York, 1958.

Chubb, T. A., Personal Communication, 1970.

CIRA 1965, COSPAR International Reference Atmosphere, North Holland Publishing Co., Amsterdam, 1965.

Cohen, H. and R. Narcisi, (1964), Cited in "Molecular Oxygen Distribution in the Upper Atmosphere, 2," (Jursa, A., M. Nakamura, and Y. Tanaka), J. Geophys. Res., Vol. 70, pp. 2699-2702, 1965.

Cooley, J. W. and J. W. Tukey, "An Algorithm for the Machine Calculation of Complex Fourier Series," Math. of Computation, Vol. 19, pp. 297-301, 1965.

Grobecker, A. J., Vehicle Characteristics, North American Aviation, Inc., Space Division Report SD 66-1338-9, June 1967a.

Grobecker, A. J., Ion Chambers for Detection of Ultraviolet, North American Aviation, Inc., Space Division Report SD 66-1338-7, June 1967b.

Grobecker, A. J., Ion Chambers for Detection of Soft X-Rays, North American Aviation, Inc., Space Division Report SD 66-1338-8, June 1967c.

Grobecker, A. J., The Sun in February 1966, NAA SD 66-1338-1, July 1967d.

Grobecker, A. J., "X-Ray and EUV Photometric Determinations of the Latitudinal and Temporal Variations of the Total Particle and O_2 Molecule Density Distribution in the Region 70-150 Kilometers in the Earth's Atmosphere" (University Microfilms, Ann Arbor, Michigan, Order No. 68-3259, Vol. 28, No. 9, p. 3757-B, 1968), Ph.D. Thesis, Univ. of Calif., L. A., 1967e.

Gross, J., D. Offermann and U. von Zahn, "Neutral Particle Densities in the Lower Thermosphere as Measured by Mass Spectrometers above Fort Churchill and Sardinia," Space Research, VIII, pp. 920-925, 1967.

Hinteregger, H. E., L. A. Hall and G. Schmidtke, "Solar XUV Radiation and Neutral Particle Distribution, July, 1963 Thermosphere," Space Science V, pp. 1175-1189, North Holland Publishing Company, 1964.

Jursa, A., M. Nakamura and Y. Tanaka, "Molecular Oxygen Distribution in the Upper Atmosphere," J. Geophys. Res., Vol. 68, p. 6145, 1963.

Jursa, A., M. Nakamura and Y. Tanaka, "Molecular Oxygen Distribution in the Upper Atmosphere, 2," J. Geophys. Res., Vol. 70, p. 2699, 1965.

Kochanski, A., "Atmospheric Motions from Sodium Cloud Drifts," J. Geophys. Res., Vol. 69, p. 3651, 1964.

Kochanski, A., "Atmospheric Motions from Sodium Cloud Drifts at Four Locations," Monthly Weather Rev., Vol. 94, p. 199, 1966.

Kreplin, R. W., and B. N. Gregory, "Solar X-Ray Monitoring During the IQSY," NRL Memo, 19 July 1963.

Kreplin, R. W., "Final Data and Calibration for the Explorer 30, NRL SOLRAD 8, X-Ray Monitoring Experiment," NRL Memo, 24 Jan. 1966.

Little, G. and H. Leinbach, "The Riometer--A Device for the Continuous Measurement of Ionospheric Absorption," Proc. IRE, Vol. 47, p. 315, 1959.

Lockey, G. W. A., B. H. Horton and B. Rofe, "Satellite Measurement of the Upper Atmospheric Molecular Oxygen Densities," Nature, Vol. 223, pp. 387-388, 1969.

McClinton, A. and R. W. Kreplin, Personal Communication, 14 Feb. 1967.

Mauersberger, K., D. Muller, D. Offermann and U. von Zahn, "A Mass Spectrometric Determination of the Neutral Constituents in the Lower Thermosphere above Sardinia," J. Geophys. Res., Vol. 73, p. 1071, 1965.

Nier, A. O., J. H. Hoffman, C. Y. Johnson and J. C. Holmes, "Neutral Composition of the Atmosphere in the 100-200 Kilometer Range," J. Geophys. Res., Vol. 69, No. 5, pp. 979-989, 1 March 1964.

Nier, A. O., H. J. Hoffman, C. Y. Johnson and J. C. Holmes, "Neutral Constituents of the Upper Atmosphere: The Minor Peaks Observed in a Mass Spectrometer," J. Geophys. Res., Vol. 69, No. 21, pp. 4629-4636, 1 Nov. 1964.

Quessette, J. A., "On the Measurement of Molecular Oxygen Concentration by Absorption Spectroscopy," J. Geophys. Res., Vol. 75, pp. 838-844, February 1970.

Schlichting, H., Boundary Layer Theory, 4th Ed., McGraw-Hill, Inc., New York, 1960.

Shimazaki, Tatsuo, "Dynamic Effects on Height Distributions of Neutral Constituents in the Earth's Upper Atmosphere: A Calculation of Atmospheric Model between 70 km and 500 km," J. Atmos. & Terr. Phys., Vol. 30, pp. 1279-1292, 1968.

Swider, W., "The Determination of the Optical Depth at Large Solar Zenith Distances," Planetary and Space Science, Vol. 12, pp. 761-782, Pergamon Press, New York, 1964.

Tchen, C. M., "Cascade Theory of Turbulence," Proc. Symposium Adv. Problems in Fluid Mechanics, Poland; Fluid Mechanics Transactions, 1969.

Tchen, C. M., "Effect of Turbulent Motions on the Transport of Molecular Constituents with Chemical Reactions in the Upper Atmosphere," submitted for publication August 1970.

U. S. Standard Atmosphere 1962, Government Printing Office, Washington, D. C., 1962.

U. S. Department of Commerce, Compilations of Solar Geophysical Data, ESSA-ITSA Reports, Feb-Oct, 1966.

Watanabe, K., "Ultraviolet Absorption Processes in the Upper Atmosphere," Advances in Geophysics, Vol. 5, pp. 153-221, (H. E. Landsberg, J. van Miegham, eds.), Academic Press, New York, 1958.

Wright, J. W., Personal Communication, 1966.

Zahn, von U. and J. Gross, "Messungen von Dichte, Zusammensetzung und Temperatur der neutralen Atmosphare im Bereich von 110 bis 160 km Hohe," Physikalisches Institut der Universetat Bon, August 1968.

BLANK PAGE

APPENDIX A

SOLAR EMISSION CONSTANCY

In designing an experiment that spans an interval of time, it is desirable to ensure, where possible, that only intended variables change. In the NC7.178, 180 and 181 experiments, the two variables of the problem were conceived to be the hour angle of the sun and the latitude of the observations. The range of time between the first and last launching was nearly seven hours. It was desirable, therefore, to establish whether large transients other than those due to changing hour angle of the sun and latitude of observation occurred in the interval from about 0700 to 1400 CST on 21 February 1966. Specifically, it was hoped that during this interval of time no sudden change in solar activity would occur to produce a sharp change in the normal quiet state of the terrestrial atmosphere.

Several types of observations determined that solar emission was comparatively constant during the period of the experiments. These included observations by satellite, ionosonde, and a world-wide riometer network.

1. SATELLITE OBSERVATIONS

The X-ray monitoring satellite Explorer 30, which provided numerous measurements of solar X-ray emissions during 1966 (Kreplin, 1966), has measured radiation in the 1-8, 8-16, and 44-60Å wave bands.

Data in Fig. A-1 from McClinton and Kreplin (1967) show solar flux measured by the satellite on the day of the NC7.178, 180 and 181 launches. This flux was essentially constant between 1300 and 2000 GMT.

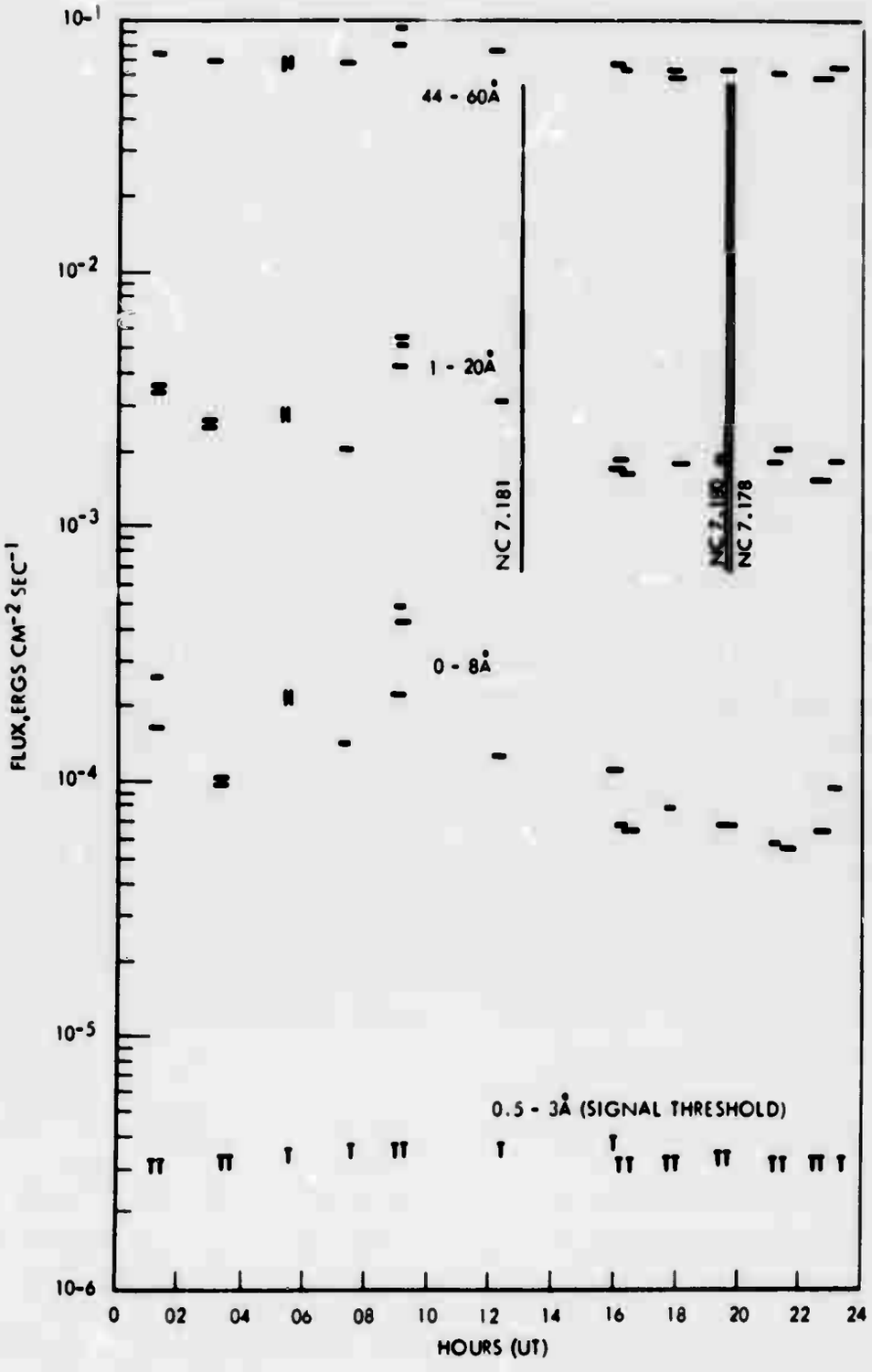

FIGURE A-1. X-Ray Flux, Explorer 30 Satellite, 21 February 1966 (McClinton and Kreplin, 1967)

2. RIOMETER OBSERVATIONS

Riometers of a type described by Little and Leinbach (1959) are located at various stations throughout the world, approximately on the 75th meridian west and on the geomagnetic equator. They are operated under the general coordination of the AFCRL Laboratory, Bedford, Massachusetts (Raymond J. Cormier, Principal Investigator). The riometers, sensitive to radiation of 30 MHz, indicate changes in radiation from sources outside the earth's atmosphere, as well as changes in the degree of ionization of the atmosphere itself.

Records for a number of the stations, plotted in local sidereal time of 21 February 1966, are shown in Fig. A-2.

When compared with a plot, for each location, of average signal level for the month, the data of Fig. A-2 show that no significant absorption events occurred on 21 February 1966.

3. IONOSONDE OBSERVATIONS

The degree of atmospheric excitation may be indicated by the distribution of electron density in the atmosphere. The ionosonde is the most direct means of measuring electron density of the ionosphere from the ground.

Characteristics of the ionosonde data taken hourly during February 1966, including the day of the launches, are described generally in AFCRL Geophysics and Space Data Bulletin (1966). Detailed measurements by ionosonde at the launch sites (Fig. 26) indicate a normal diurnal change of the lower ionosphere.

4. OTHER OBSERVATIONS OF SUN AND ATMOSPHERE

Numerous other observations of the sun and the atmosphere were made (AFCRL Geophysics Space Data Bulletin, 1966, and U.S. Department of Commerce, ESSA-ITSA Reports, 1966). These imply the following conclusions concerning solar and atmospheric activity on 21 February 1966:

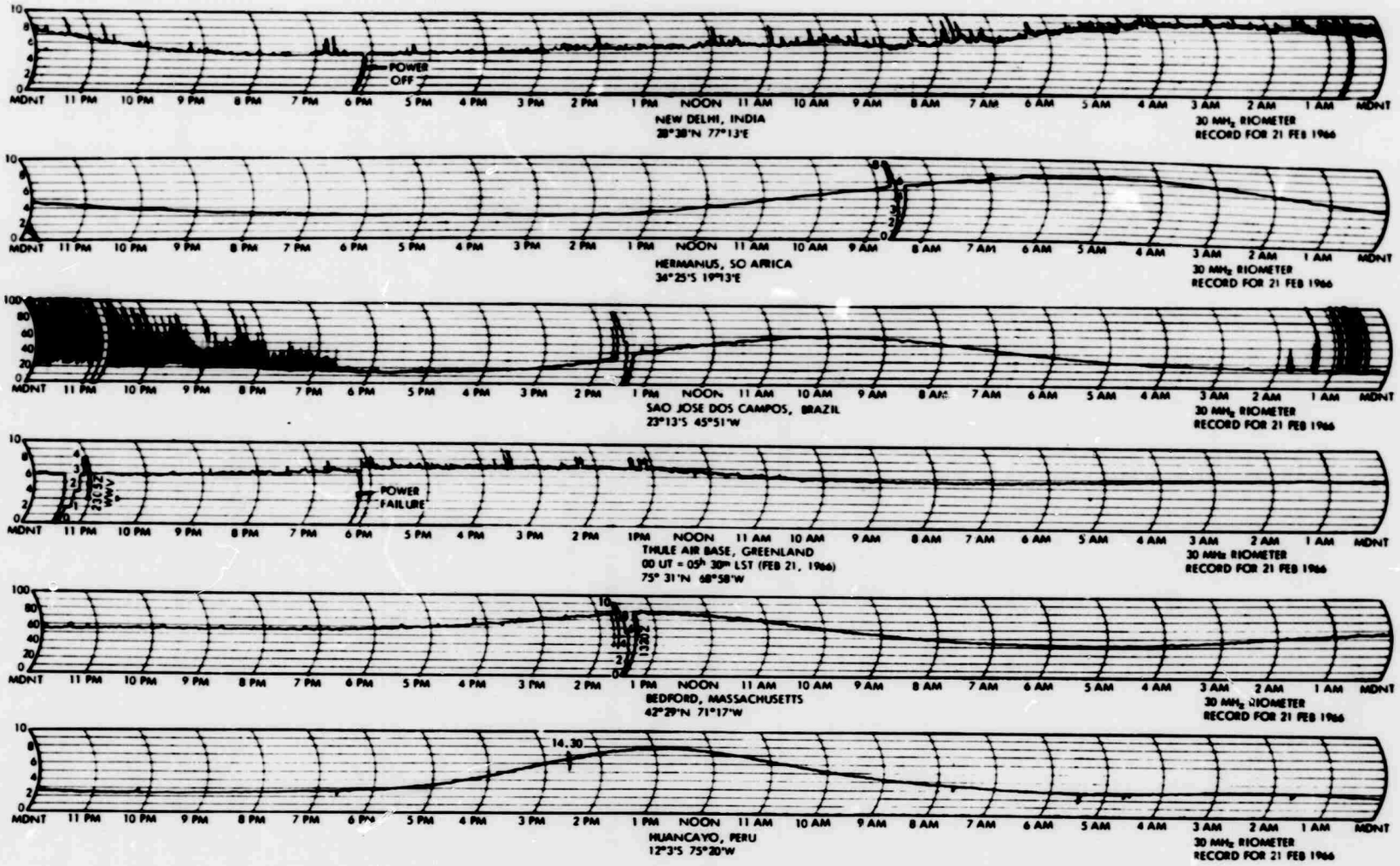

FIGURE A-2. 30-MHz Riometer Recordings for 21 February 1966

a. No unusual disturbances of solar emission occurred.

b. No strong solar-induced transients occurred in the terrestrial atmosphere. This is evidenced by the fact that the AFCRL world riometer network detected no appreciable 30-MHz absorption event.

c. A minor absorption event was observed by a 30-MHz riometer at Great Whale River, Canada, indicating the presence of some auroral activity in the period from 0130 to 2146 UT. This interval includes the times of measurements by the NC7.178, 180, and 181 experiments.

d. Electron-density profiles measured by ionosonde at the time and launch location of the NC7.178, 180, and 181 experiments appear regular.

BLANK PAGE

APPENDIX B

FRACTIONAL VARIATION OF DENSITY COMPUTATIONS

The fractional variation or coefficient of variation (ratio of standard deviation of individual density determinations to mean values) is calculated for intervals of 8 km over a part of the credible range.

For each altitude value within the desired credible range, the corresponding density value for one detector (Phase A) of some channel is denoted by DA_t and for the other detector (Phase B) by DB_t, where t takes values from 1,..., NP, and NP represents the total number of data points within the altitude range of the computation. Then:

$$AV_t = (DA_t + DB_t)/2 \qquad (B1)$$

For each altitude z_t ($t = 1,\ldots, NP$), N is determined so that

$$z_{t+N} \leq z_t + 8 \leq z_{t+N+1}$$

and

$$ER_t = \frac{\sqrt{\sum_{j=t}^{t+N} (AV_j - DA_j)^2/(N+1)}}{\sum_{j=t}^{t+N} AV_j/(N+1)} \qquad (B2)$$

A single variation value is also calculated for the entire credible range. On this basis, density errors (ratio of standard deviation to mean values) for experiment NC7.178 are shown in Fig. B-1, for NC7.180 in Fig. B-2 and for NC7.181 in Fig. B-3. Density variations, so computed, do not include systematic errors in the measurement of solar flux for which estimates have been given in the body of the report.

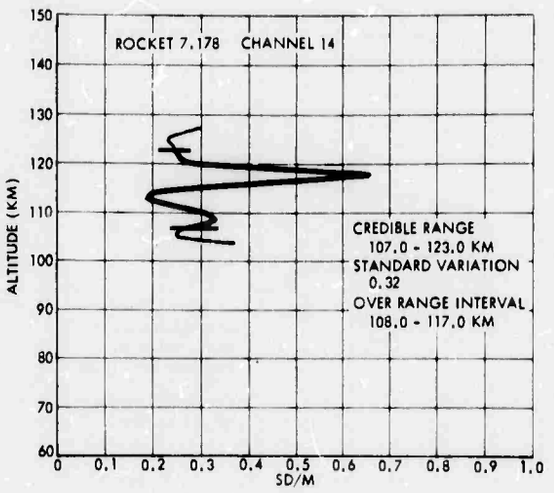

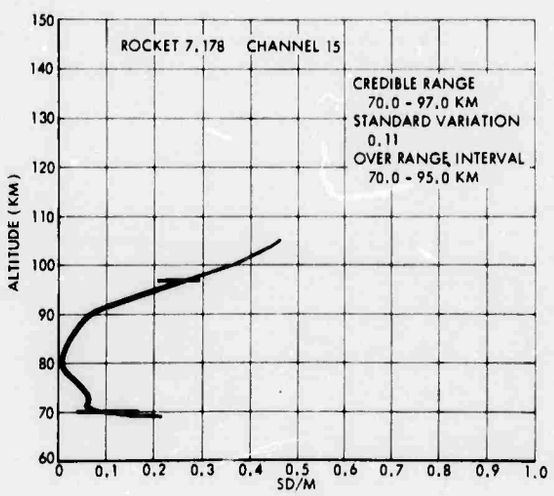

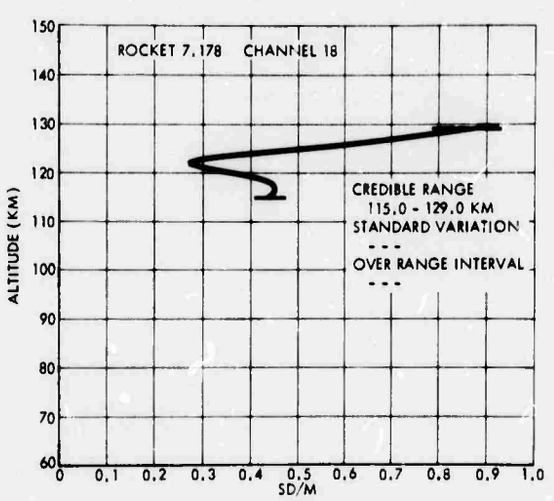

FIGURE B-1. Coefficient of Variation of Density, NC7.178

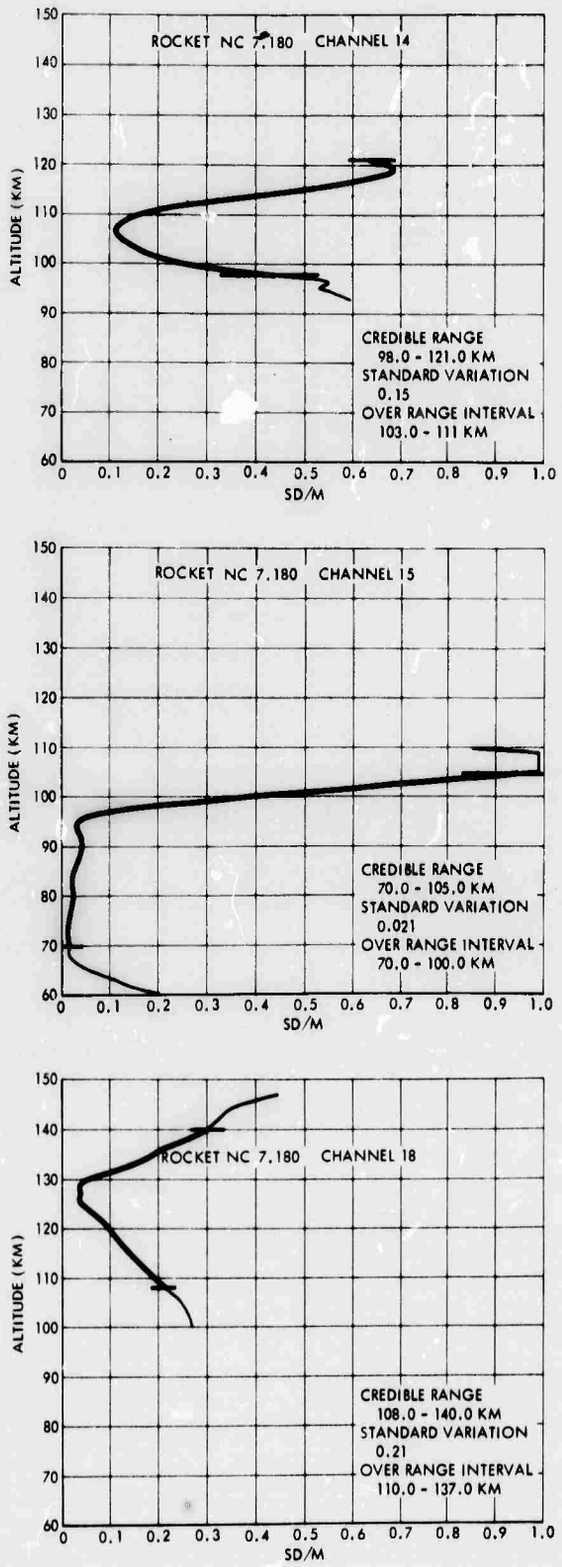

FIGURE B-2. Coefficient of Variation of Density, NC7.180

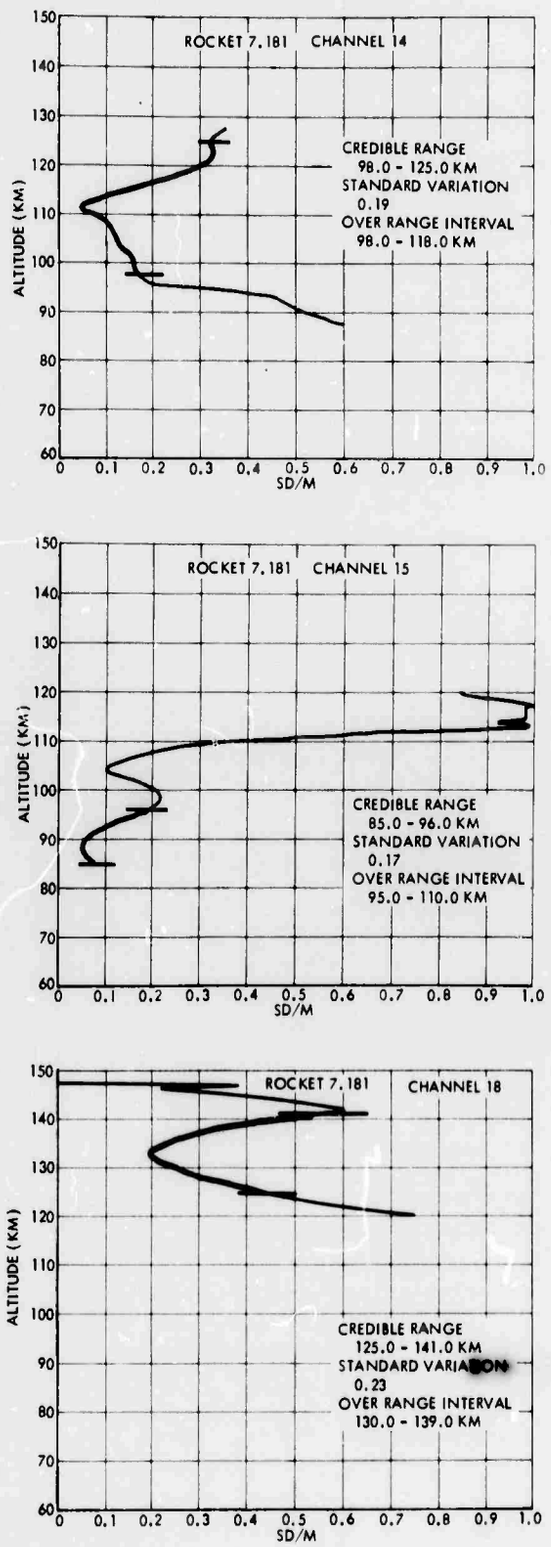

FIGURE B-3. Coefficient of Variation of Density, NC7.181